

11114
11114
0011
93045

**Design Methodology for Multi-Element High-Lift Systems on Subsonic
Civil Transport Aircraft**

R.S. Pepper and C.P. van Dam
Department of Mechanical and Aeronautical Engineering
University of California
Davis, CA 95616

Final Report

Cooperative Agreement NCC2-5042

August 1996

Abstract

The choice of high-lift system is crucial in the preliminary design process of a subsonic civil transport aircraft. Its purpose is to increase the allowable aircraft weight or decrease the aircraft's wing area for a given takeoff and landing performance. However, the implementation of a high-lift system into a design must be done carefully, for it can improve the aerodynamic performance of an aircraft but may also drastically increase the aircraft empty weight. If designed properly, a high-lift system can improve the cost effectiveness of an aircraft by increasing the payload weight for a given takeoff and landing performance. This is why the design methodology for a high-lift system should incorporate aerodynamic performance, weight, and cost.

The airframe industry has experienced rapid technological growth in recent years which has led to significant advances in high-lift systems. For this reason many existing design methodologies have become obsolete since they are based on outdated low Reynolds number wind-tunnel data and can no longer accurately predict the aerodynamic characteristics or weight of current multi-element wings. Therefore, a new design methodology has been created that reflects current aerodynamic, weight, and cost data and provides enough flexibility to allow incorporation of new data when it becomes available.

This page intentionally left blank

Table of Contents

Abstract	ii
Acknowledgments.....	iii
Table of Contents	iv
List Of Figures	vi
Nomenclature	viii
1.0 Introduction.....	1
2.0 High-Lift Configurations	4
2.1 Trailing-Edge Devices	4
2.1.1 Plain Flaps.....	5
2.1.2 Slotted Flaps	5
2.1.3 Fowler Flaps.....	7
2.2 Leading-Edge Devices	9
2.2.1 Slats.....	10
2.2.2 Krüger Flaps.....	10
3.0 Performance Requirements	16
3.1 Takeoff.....	16
3.2 Landing	18
4.0 Design Constraints	21
5.0 Computational Modeling	24
6.0 Aerodynamic Database	26
7.0 Aerodynamic Module	33
7.1 Two-Dimensional Aerodynamics	33
7.1.1 Lift.....	34
7.1.2 Drag.....	38
7.1.3 Pitching Moment.....	40
7.2 Three-Dimensional Aerodynamics	42
7.2.1 Lift.....	44

7.2.2 Drag.....	45
7.2.3 Pitching Moment.....	46
7.3 Maximum Lift Prediction	46
7.3.1 Two-Dimensional	47
7.3.2 Three-Dimensional	49
8.0 Weight Module	58
8.1 Trailing-Edge Flap Weight	59
8.2 Leading-Edge Flap Weight	61
9.0 Cost Module.....	66
10.0 Sample Application.....	70
11.0 Concluding Remarks.....	82
References.....	85
Appendix A	89
Appendix B	96

List Of Figures

Figure 1.1	-	Overview of High-Lift Module Integration	3
Figure 2.1	-	Lift Curves for Various High-Lift Airfoils	12
Figure 2.2	-	Trailing-Edge Flap Configurations	12
Figure 2.3	-	High-Lift Support Types.....	13
Figure 2.4	-	Definition of Fowler Action.....	13
Figure 2.5a	-	Usable Lift of Civil Transport Aircraft.....	14
Figure 2.5b	-	Tail-Scrape Angle of a Typical Civil Transport Aircraft.....	14
Figure 2.6	-	Various Leading-Edge Devices	15
Figure 2.7	-	Surface Disturbances Created by Leading-Edge Devices in Cruising Flight.....	15
Figure 3.1	-	FAR 25 Takeoff Requirements.....	20
Figure 3.2	-	FAR 25 Landing Requirements	20
Figure 6.1	-	Two and Three-Element Airfoil Geometries	28
Figure 6.2	-	Sample CHIMERA Grid of the NLR-7301 Two-Element Airfoil.....	28
Figure 6.3	-	NLR-7301 Pressure Distribution ($\alpha=6^\circ$, $Re=2.51 \times 10^6$)	29
Figure 6.4	-	NLR-7301 Lift Curve ($Re=2.51 \times 10^6$).....	29
Figure 6.5	-	NLR-7301 Drag Polar ($Re=2.51 \times 10^6$)	30
Figure 6.6	-	Sample CHIMERA Grid of the Douglas LB-546 Three-Element Airfoil.....	30
Figure 6.7	-	Douglas 3-Element Pressure Distribution ($\alpha=8.1^\circ$, $Re=9.0 \times 10^6$).....	31
Figure 6.8	-	Douglas 3-Element Lift Curve ($Re=9.0 \times 10^6$)	31

Figure 6.9	-	Douglas 3-Element Drag Polar ($Re=9.0 \times 10^6$).....	32
Figure 7.1	-	NLR-7301 Separation Factor.....	51
Figure 7.2	-	NLR-7301 Lift-Effectiveness	51
Figure 7.3	-	Overview of Aerodynamic Analysis.....	52
Figure 7.4	-	Part-Span-Flap Deflection Test Case.....	53
Figure 7.5	-	Part-Span-Flap Spanwise Load Distribution VTW7S1 Configuration, $\alpha=11.4^\circ$	53
Figure 7.6	-	Part-Span-Flap Spanwise Load Distribution VTW7 Configuration, $\alpha=8.5^\circ$	54
Figure 7.7	-	Swept-Wing Test Case.....	54
Figure 7.8	-	Swept-Wing Lift Distribution Plain Wing Model, $C_L=0.4$	55
Figure 7.9	-	Swept-Wing Lift Distribution Cambered & Twisted Wing Model, $C_L=0.4$	55
Figure 7.10	-	Procedure for Calculating Pitching Moment	56
Figure 7.11	-	Increment In Stall Angle Due to Various L. E. Devices.....	56
Figure 7.12	-	Maximum Lift Estimation Using Critical Section Approach.....	57
Figure 8.1	-	Trailing-Edge Weight Correlations for Various Aircraft.....	65
Figure 8.2	-	Leading-Edge Weight Correlations for Various Aircraft.....	65
Figure 10.1	-	Lift Curves of Sample Test Cases.....	81
Figure 10.2	-	Drag Polars of Sample Test Cases	81

Nomenclature

α	-	angle of attack (rad)
$a_{1,2, \dots, \text{etc.}}$	-	empirical constants
α_δ	-	lift-effectiveness of flap $\left(\frac{\partial \alpha}{\partial \delta_{TE}} \right)$
α_o	-	angle of attack at zero lift (rad)
AR	-	aspect ratio of wing
$b_{1,2, \dots, \text{etc.}}$	-	empirical constants
c	-	reference cruise chord length in the streamwise direction (ft)
χ	-	separation factor of flap
c'	-	extended chord length due to system deployment (ft)
$c_{1,2, \dots, \text{etc.}}$	-	empirical constants
C_D	-	drag coefficient based on reference area
C_d	-	local drag coefficient based on local reference chord
$C_{d_{\min}}$	-	minimum drag coefficient
C_L	-	lift coefficient of wing based on the reference area
C_l	-	local lift coefficient based on the local reference chord
C_{L_α}	-	lift curve slope of wing (rad ⁻¹)
C_{l_α}	-	local lift curve slope of airfoil (rad ⁻¹)
$C_{l_\alpha}^{\text{clean}}$	-	local lift curve slope of cruise airfoil (rad ⁻¹)
C_{l_δ}	-	lift-effectiveness of flap (rad ⁻¹)
$C_{l_\delta}^{\max}$	-	maximum lift-effectiveness of flap (rad ⁻¹)
$c_{LE/TE}$	-	leading or trailing-edge device chord length (ft)
$C_{l_{\max}}$	-	local maximum lift coefficient based on the reference chord
$C_{L_{\max}}$	-	maximum lift coefficient of wing based on the reference area
$C_{l_{\min}}$	-	lift coefficient at minimum drag
C_m	-	local pitching moment coefficient based on the local reference chord
C_M	-	pitching moment coefficient of wing based on the reference area
$d_{1,2, \dots, \text{etc.}}$	-	empirical constants
$\Delta\alpha_{\max}$	-	change in stall angle due to deployed leading-edge device (rad)
Δc	-	increase in chord due to Fowler action (ft)
ΔC_L	-	increment in lift (linear region) due to high-lift devices
$\Delta C_{L_{\max}}$	-	maximum increment in lift due to high-lift devices
$\delta_{LE/TE}$	-	leading or trailing-edge device deflection angle (rad)
ΔS_{Fowler}	-	increase in flap area due to Fowler motion (ft ²)
ϵ_w	-	wing twist angle (rad)
f_1	-	Fowler action function of 1 st flap element
f_2	-	Fowler action function of 2 nd flap element
γ	-	flight-path angle of aircraft (rad)

$\eta_{LE/TE}$	-	leading/trailing-edge device span break locations (% of wing span)
k_p	-	profile drag polar constant
Λ	-	quarter chord sweep angle of wing (rad)
λ	-	wing taper ratio
L/D	-	lift-to-drag ratio of wing
M	-	freestream Mach number based on V_2 for takeoff and V_A for landing
θ	-	fuselage angle (rad)
$\theta_{tail-scraper}$	-	tail-scraper angle of fuselage (rad)
Re	-	Reynolds number based on V_2 for takeoff and V_A for landing
S	-	wing reference area (ft ²)
s_1	-	shroud length of main element
s_2	-	shroud length of 1 st flap element
S_{LE}	-	planform area of leading edge flap (ft ²)
S_{TE}	-	planform area of stowed flap (ft ²)
t/c	-	maximum thickness ratio of cruise airfoil
U/C	-	landing gear
V_1	-	decision speed (kts)
V_2	-	takeoff climb speed (kts)
V_A	-	approach speed (kts)
V_{LOF}	-	lift-off speed (kts)
V_{MC}	-	minimum control speed (kts)
V_{MCG}	-	minimum control speed on the ground (kts)
V_{MS}	-	minimum dynamic stall speed (kts)
V_{MU}	-	minimum unstick speed (kts)
V_R	-	rotation speed (kts)
$V_{S_{1g}}$	-	stall speed of aircraft in steady flight (kts)
V_{TD}	-	touch-down speed (kts)
W_L	-	maximum landing weight (lb)
$x_{1,2, \dots, etc.}$	-	empirical exponents
x_{ac}	-	aerodynamic center of airfoil section (ft)
x_{cp}	-	center of pressure of airfoil section (ft)

1.0 Introduction

The design of an efficient high-lift system remains as challenging today as it was twenty years ago when A.M.O. Smith wrote his enlightening papers on high-lift aerodynamics.^{1,2} Modern civil transport aircraft require complex multi-element high-lift systems to meet stringent performance criteria during the takeoff and landing phases of flight. In the current competitive market place, new aircraft designs are driven to simpler, more efficient high-lift systems that provide improved aerodynamic performance in terms of increased maximum lift coefficient, $C_{L_{max}}$, increased lift-to-drag ratio, L/D , or increased lift coefficient, C_L , for a given angle of attack and flap setting. Garner and his co-workers at Boeing³ present excellent examples illustrating the importance of a high-lift system in the design of a B777 type of aircraft:

1. $\Delta C_L = +0.10$ for a constant angle of attack on approach for landing reduces the pitch attitude angle by about one degree. For a given aircraft geometry and landing-gear location this allows a reduction in landing-gear height and an associated weight reduction of 1,400 lb.
2. $\Delta C_{L_{max}} = +1.5\%$ at a fixed approach speed results in an increase in payload of 6,600 lb.
3. $\Delta(L/D) = +0.10\%$ on takeoff results in an increase in payload of 2,800 lb.

These examples illustrate the enormous importance of a well designed and engineered high-lift system in the overall development process of a subsonic civil transport aircraft. However, these systems also increase the structural weight, complexity, maintenance requirements, and cost of an aircraft. Thus, the designer is faced with the task of developing such a high-lift system that allows the airplane to meet

the takeoff and landing performance requirements while minimizing the weight and cost of the airplane.

This report presents a design methodology for multi-element high-lift systems for subsonic civil transport aircraft that includes aerodynamic performance, structural weight considerations, system complexity, and cost. The methodology is designed to be compatible with ACSYNT⁴, a multidisciplinary computer-aided aircraft conceptual design tool. Consequently, important considerations are (1) to find a reasonable compromise between the CPU requirements (on current generation workstations) of the high-lift module and the accuracy of the predictions by the module and (2) to provide enough flexibility to enhance the capabilities of the high-lift module when more powerful hardware and software becomes available.

It is envisioned that this methodology will be integrated into ACSYNT as illustrated in figure 1.1. Once the development of the aerodynamic database for double and triple-slotted flaps is finished, the high-lift module can be used in the 1st level of design as described in this report. Given the initial concept and mission requirements, iteration is required to find the optimum initial high-lift configuration based on general, or historical data. Subsequent levels of design should then take advantage of computational fluid dynamics (CFD), experimental fluid dynamics (EFD), or flight data to more accurately model the configuration selected from the 1st level. When provided with more complete aircraft geometry and given data that is based on a specific configuration, the methodology can then converge on an optimum preliminary high-lift configuration.

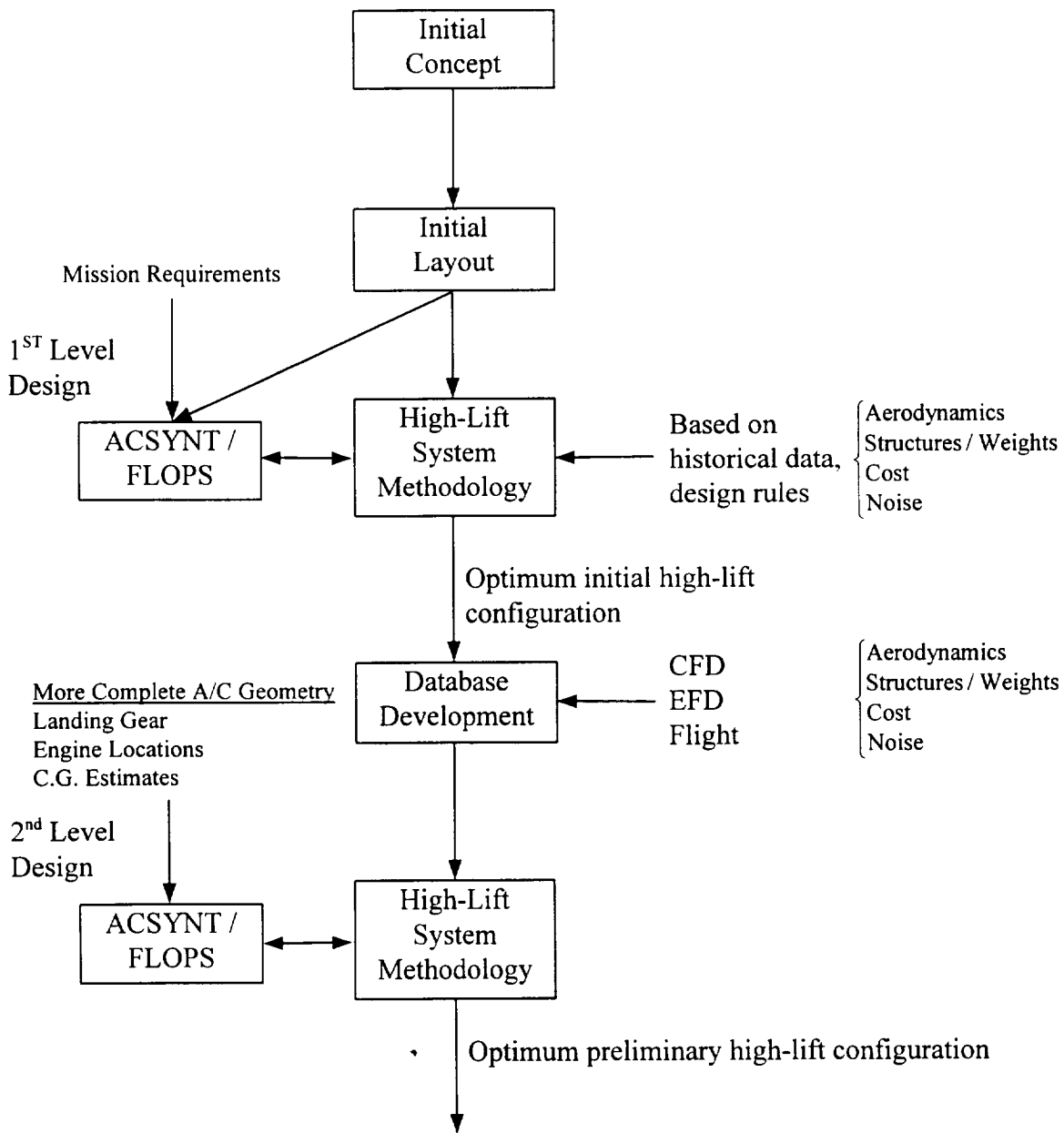


Figure 1.1 Overview of High-Lift Module Integration

2.0 High-Lift Configurations

High-lift systems consist of leading and trailing-edge devices. Leading-edge devices increase the maximum lift of an airfoil by delaying its stall angle, $\Delta\alpha_{\max}$, as shown in figure 2.1. This change in the stall angle is relatively constant for airfoils both with and without trailing-edge devices.⁵ Trailing-edge devices produce a lift increment, ΔC_L , and as illustrated in figure 2.1 the magnitude of this increment is approximately independent of a leading-edge device.

2.1 Trailing-Edge Devices

A trailing-edge device generates additional lift through an increase in the effective rearward camber of an airfoil. It is desirable to create a flap that produces a large increase in lift while maintaining a high lift-to-drag ratio, L/D , in order to enhance both the takeoff and landing performance of an aircraft. There are many trailing-edge devices employed today, but the most common are the plain flap, slotted flap, and Fowler flap. Figure 2.2 shows examples of these various flap configurations.

In addition to the various flap configurations, there are three widely used support types: hinge, linkage, and track supports. These systems, which are illustrated in figure 2.3, are used on the various configurations to deploy the flaps to their proper deflection angles and provide necessary structural support. The hinge support is the simplest of these support types, but it also has the worst aerodynamic performance. Since the flap

kinematics are restricted by the hinge position, the flap can only be optimized at one deflection angle. The linkage and track supports are more complex, but they can provide optimum flap settings at multiple deflection angles.

2.1.1 Plain Flaps

The plain flap consists of a hinged trailing-edge with a gap that is usually sealed to reduce leakage. It is the simplest of all trailing-edge devices but is also the least efficient in terms of the lift increment it can generate without flow separation. Plain flaps are commonly used as high-lift devices on general aviation aircraft which have low wing loadings. On civil transport airplanes plain flaps are rarely used except as control surfaces.

2.1.2 Slotted Flaps

Slotted flaps offer improved efficiency over plain flaps due to a delay in flow separation. To better understand this phenomenon, we must review A.M.O. Smith's classic papers on high-lift aerodynamics^{1,2}. Previously, the effects of slots in multi-element airfoils were incorrectly attributed to boundary-layer control through blowing. Smith argues that the principal effect of a slot is to delay flow separation through inviscid interactions.

Smith asserts that gaps have five primary effects on multi-element airfoils. The peak pressure on a downstream element is reduced by an induced velocity created by the

circulation of a forward element. This is referred to as the "*slat effect*", and it delays flow separation by relieving pressure recovery. In turn, the "*circulation effect*" induces a greater circulation on the forward element because its trailing-edge lies in a region of high velocity at the leading-edge of the adjacent downstream element. Since the trailing-edge of the forward element lies in a high velocity region, the boundary layer is shed at a high velocity. This "*dumping effect*" delays flow separation by reducing the pressure rise over the airfoil and allows for "*off-the-surface pressure recovery*" which is much more efficient than recovery in contact with a wall. Finally, each surface benefits from a "*fresh boundary-layer*" which originates from the leading-edge of each element. Thus, multi-element airfoils allow for a more efficient pressure recovery, since thin boundary layers can withstand stronger adverse pressure gradients than thick ones before separating.

While these five effects primarily influence the inviscid nature of the flow, they also have important secondary viscous effects. It is this balance between the inviscid and viscous nature of multi-element airfoils that necessitates the optimization of gap size. The inviscid effects favor smaller gaps, while the viscous effects require larger slots. One problem associated with this trade-off is found in confluent boundary layers. If the gaps are not designed properly the wakes will merge resulting in exceptionally thick boundary layers.

2.1.3 Fowler Flaps

Improved performance can also be obtained if a flap creates Fowler action, or rearward translation of the flap. Here, Fowler action is defined as the measure of the change in position of the leading-edge of the flap in the plane of the chord of the fore element. This is illustrated in figure 2.4 and is expressed as:

$$\text{Fowler action} = \Delta c = s_1 + s_2 \quad (1)$$

The extended chord of an airfoil can then be defined as the length of the cruise airfoil plus the Fowler action:

$$c' = c + \Delta c \quad (2)$$

This extension in wing area increases the airfoil's lift curve slope, generating more lift without a significant increase in drag:

$$C_{l_\alpha} = C_{l_{\alpha \text{clean}}} \frac{c'}{c} \quad (3)$$

However, Fowler action also produces an increase in the nose-down pitching moment which makes the aircraft more difficult to trim.

Of all slotted trailing-edge devices, the single-slotted Fowler flap is the simplest and most efficient. It is a superior device for takeoff because it has the best L/D, but designers often cannot employ wings with single-slotted flaps because their usable lift is inadequate for takeoff and/or landing. In such cases a multi-element flap is required.

The usable lift problem faced in the design of civil transport airplanes is depicted for the landing case in figure 2.5. The landing distance of an airplane is governed by its

weight and approach speed, assuming that the wing area is fixed and determined by cruise requirements. The Federal Airworthiness Requirements stipulate that the minimum approach speed V_A equals $1.22V_{S_{1g}}$, where $V_{S_{1g}}$ represents the 1-g stall speed of the airplane in the landing configuration. For a given weight and landing distance the approach speed is more-or-less fixed, and the lift coefficient during landing approach is:

$$C_{L_A} = W_L / \left(\frac{1}{2} \rho V_A^2 S \right) \leq C_{L_{\max}} / (1.22)^2 \quad (4)$$

In figure 2.5a this lift coefficient is marked. During approach, airplane angle of attack is governed by the following equation for steady flight:

$$\alpha = \theta - \gamma \quad (5)$$

where a typical glide slope angle is $\gamma = -3^\circ$. For many configurations the maximum attitude angle is severely limited by the tail scrape angle (Fig. 2.5b) and, consequently $\alpha_{\text{limit}} = \theta_{\text{tail-scrape}} + 3^\circ$ (Fig. 2.5a). Hence, the combination of a given approach speed and a limited angle of attack may force the designer to select a more complex high-lift system as shown in figure 2.5a.

Further delay of flow separation at higher flap deflections, an additional increase in effective camber, and a potential for greater Fowler action are produced with additional flap elements. With all of these benefits combined a multi-element flap is able to generate a higher maximum lift. It also has a larger usable lift at lower angles of attack which may be important if the fuselage angle is restricted on takeoff or landing. But this increase in lift comes with a price, for the efficiency, or L/D , is reduced with each additional flap element. Structural complexity also increases with the number of elements, so multi-element flaps become more costly to manufacture and maintain

2.2 Leading-Edge Devices

Leading-edge devices are used primarily to delay the onset of stall by reducing the peak velocity in the leading-edge region of the main element. This corresponds to an increase in $C_{l_{max}}$ due to a shift in the stall angle. Slats and Krüger flaps are the most widely used leading-edge devices in industry today. The various available configurations are illustrated in figure 2.6.

There is some disagreement on which configuration provides the highest maximum lift or the lowest drag. Wedderspoon⁶ cites that a vented slat was chosen over a sealed folding bullnose Krüger for the Airbus 320 because it generated a higher maximum lift, but he does not mention if a vented Krüger flap was investigated. Woodward and Lean⁵ argue that vented Krüger flaps produce considerably higher maximum lift than vented slats and that sealed Krügers produce higher maximum lift than sealed slats. Such inconsistencies in opinions indicate that these devices are not fully understood. Clearly, more research must still be conducted to better understand the aerodynamics of leading-edge devices. It appears that slats and Krüger flaps have similar aerodynamic performance if properly designed.

In this paper, Krüger flaps and slats are considered to have the same lifting effectiveness but slightly different maximum lift capabilities. For the purposes of this methodology, the focus is placed on the flap position rather than on the configuration type. Slotted, or vented, leading-edge devices have high maximum lift capabilities. As a

result these devices produce higher drag, so they are best utilized during landing.

Conversely, sealed leading-edge devices have lower maximum lift which produce less drag and should be used during the takeoff phase.

2.2.1 Slats

A slat offers more flexibility than a Krüger flap. It generally has three settings: stowed, takeoff, and landing. The tracks are constructed to optimize the configuration for each maneuver, so the slat is sealed for takeoff and vented for landing.

2.2.2 Krüger Flaps

There are several types of Krüger flaps available: simple Krügers, folding bullnose Krügers, and variable camber Krügers, and each configuration can be either sealed or vented. The primary difference between this leading-edge device and a slat is the support structure. Krüger flaps are hinged and stow on the lower surface of the airfoil, while slats deploy from the leading-edge of the airfoil on tracks. The Krüger's hinged support does not allow a multitude of position settings, so it must be either retracted or extended. It is up to the designer to optimize the flap for takeoff or landing. Generally, the flap is vented if landing is the dominant maneuver and sealed if takeoff requirements govern the design.

One advantage of the Krüger flap is that it can be applied to a wing with laminar flow technology. Since the Krüger flap is stowed along the lower surface of the wing, it

doesn't disturb the flow over the critical upper surface of the wing in cruise flight (Fig. 2.7). The presence of irregularities on the upper surface created by the trailing-edge of a retracted slat will trip a flow from laminar to turbulent and subsequently cause adverse effects on the performance. For this reason slats can not be used on laminar flow wings.

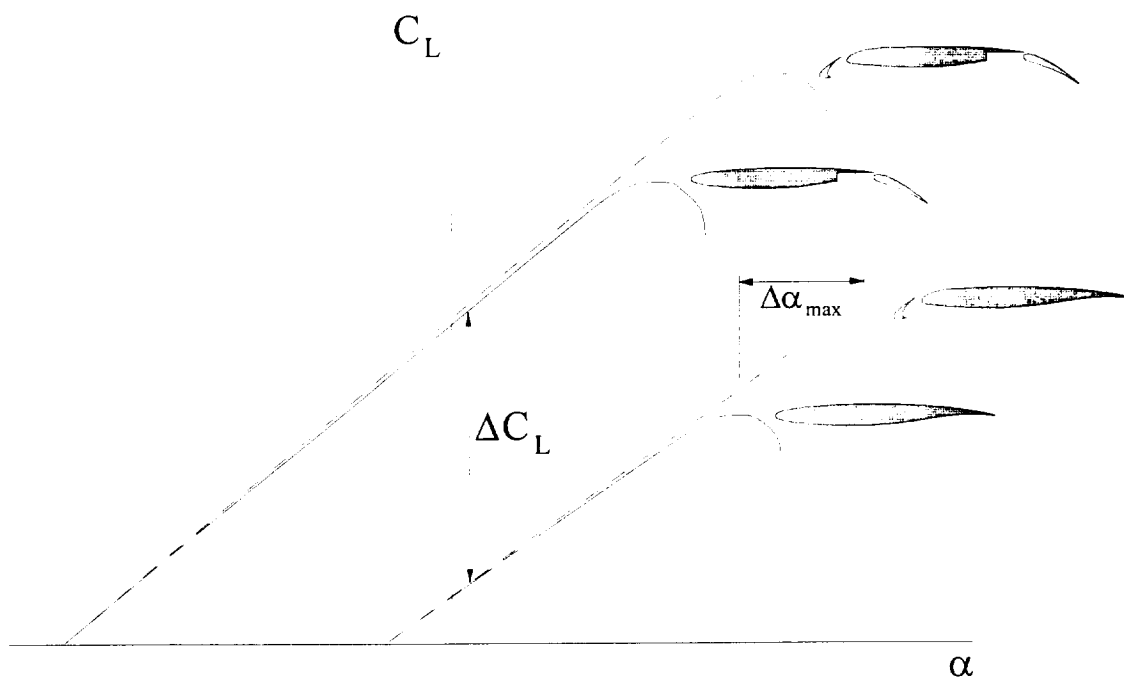


Figure 2.1 Lift Curves for Various High-Lift Airfoils

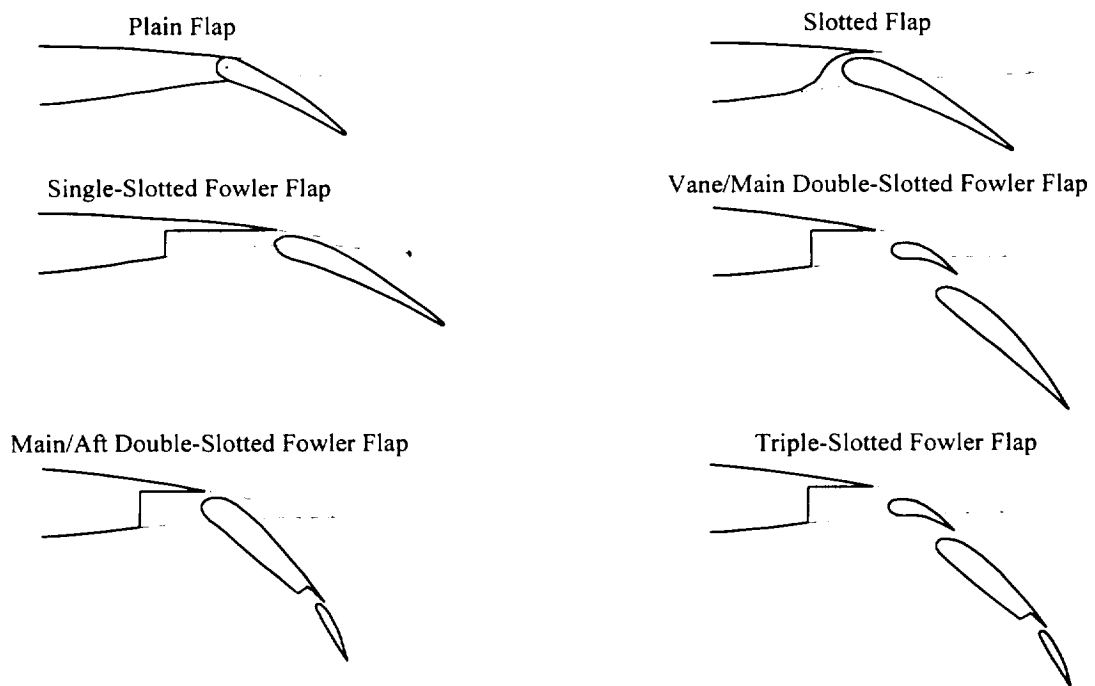


Figure 2.2 Trailing-Edge Flap Configurations

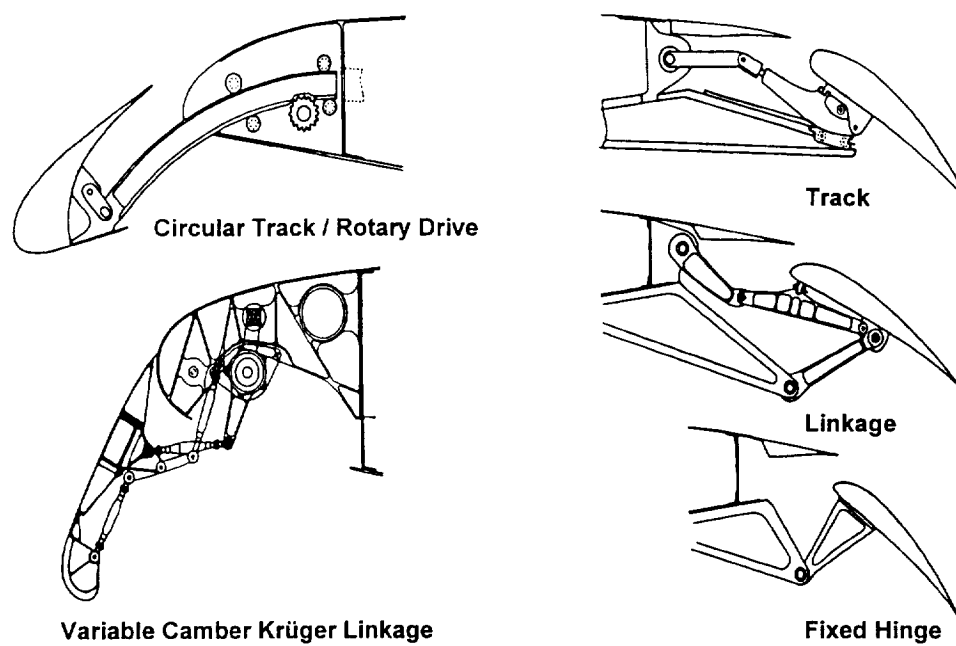


Figure 2.3 High-Lift Support Types
(adapted from Ref. 7)

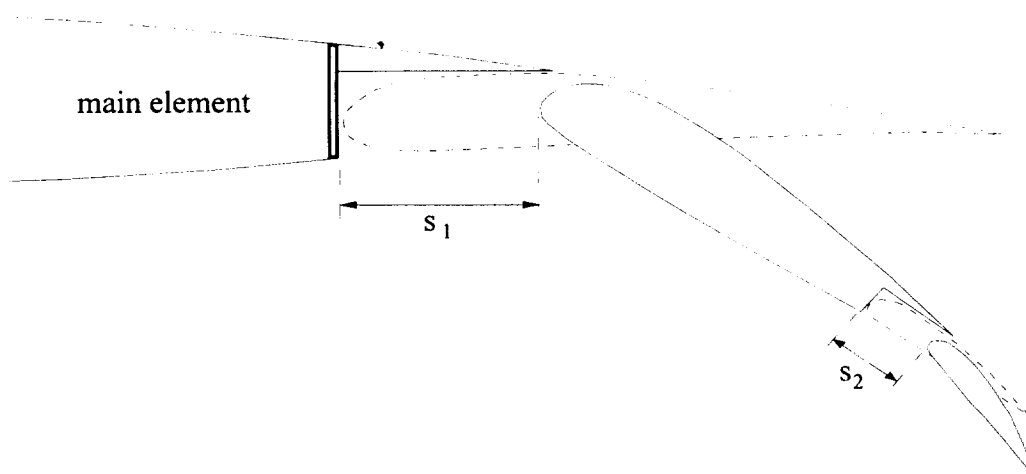


Figure 2.4 Definition of Fowler Action

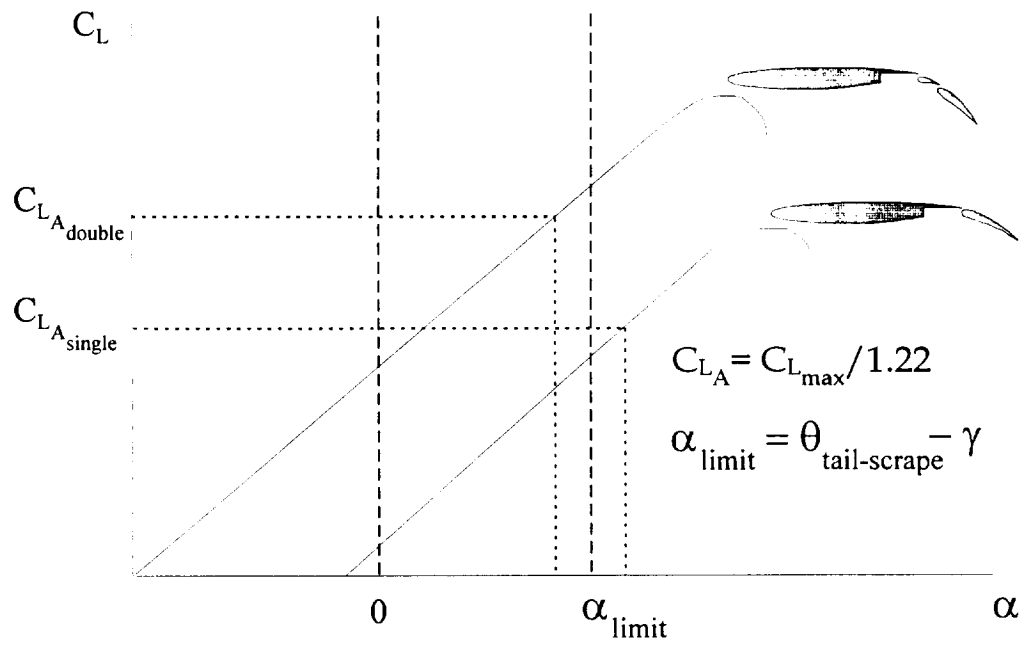


Figure 2.5a Usable Lift of Civil Transport Aircraft

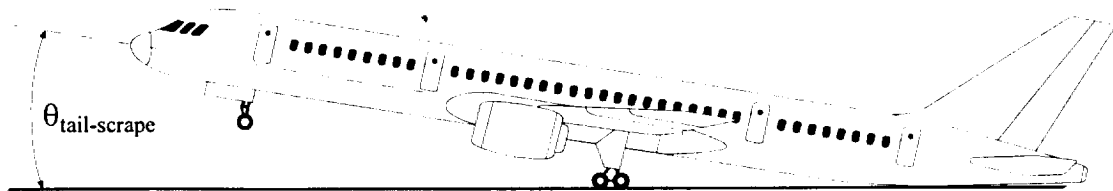


Figure 2.5b Tail-Scrape Angle of a Typical Civil Transport Aircraft

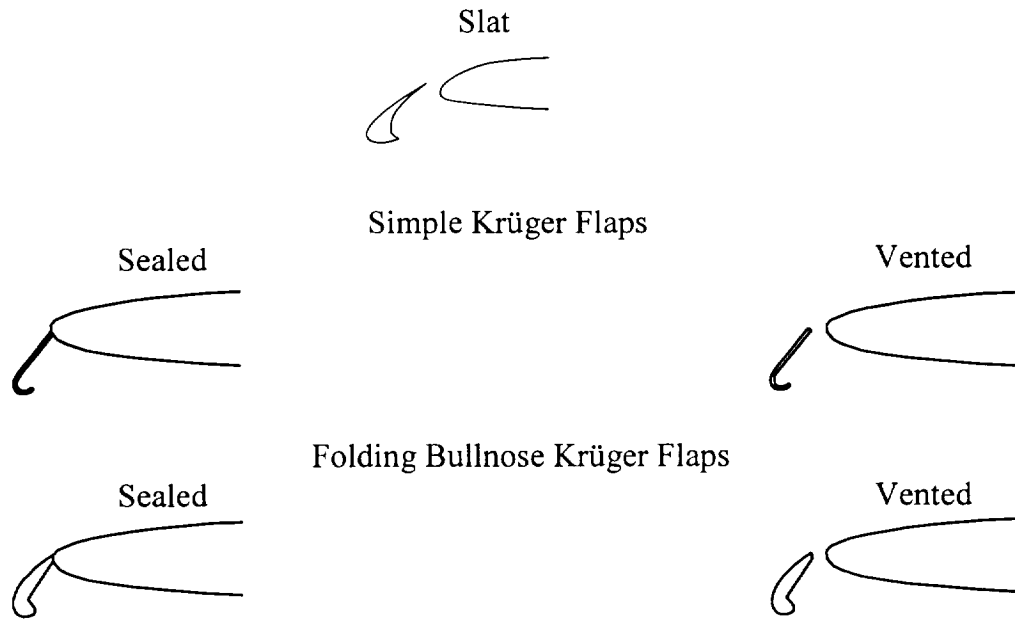


Figure 2.6 Various Leading-Edge Devices

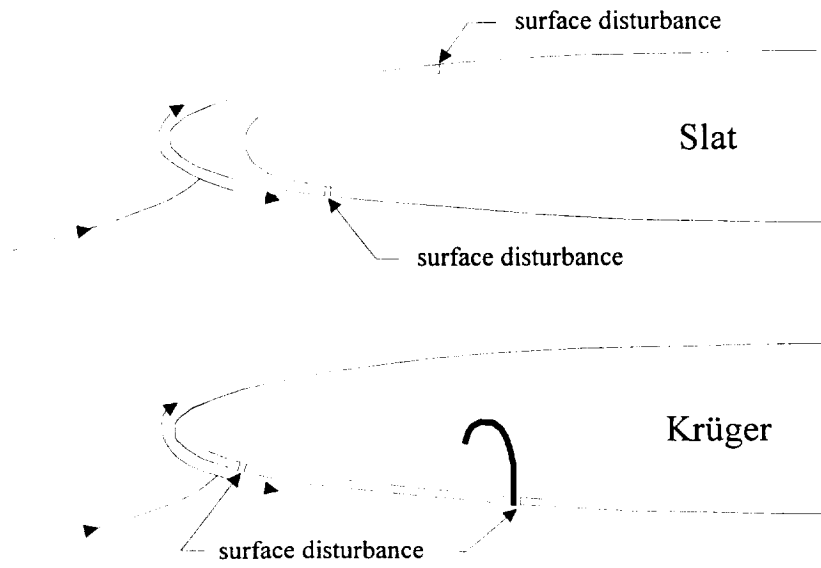


Figure 2.7 Surface Disturbances Created by Leading-Edge Devices In Cruising Flight

3.0 Performance Requirements

The takeoff and landing performance of a subsonic civil transport aircraft is governed by the requirements listed in the Federal Airworthiness Regulations (FAR) Part 25. These regulations specify minimum speeds, field lengths, and rates of climb that an airplane must maintain during a takeoff or landing maneuver. The high-lift system must ensure that the aircraft complies with these operating rules given basic fixed parameters such as wing loading and thrust loading.

3.1 Takeoff

Takeoff performance is characterized by the balanced field length and climb gradient of an aircraft. As illustrated in figure 3.1, the maneuver is divided into three segments: ground roll and rotation, lift-off and first segment climb, and second segment climb. There is also a final climb segment at 1500 feet, but this maneuver is performed with retracted high-lift devices.

The ground run ends when the aircraft rotates at a specified speed and then lifts off after the speed reaches 1.1 (1.05 with one engine out) times the minimum unstick speed V_{MU} , where V_{MU} represents the minimum airspeed at which the airplane can safely lift off and continue the takeoff with its critical engine inoperative. This maneuver is generally a function of the maximum usable lift (not the absolute maximum lift), because an aircraft's rotation angle and, thus, angle of attack is restricted by the fuselage's tail-

scrape angle. The effects of this limitation must be taken into consideration when choosing a high-lift configuration, since the addition of another flap element may be required to increase the usable lift.

The aircraft must now reach its takeoff climb speed V_2 before it arrives at the screen height of 35 feet. This speed must equal or exceed 1.1 times the minimum control speed and 1.2 times the minimum dynamic stall speed. Generally the latter constraint corresponds to 1.13 of $V_{s_{1g}}$, the stall speed in steady flight. This implies that the lift coefficient must be equal to or less than $C_{L_{max}}/1.13^2$. Thus, a high maximum lift coefficient is essential to obtain a low takeoff climb speed.

The second segment climb begins when the landing gear is retracted. At this point the aircraft must maintain an airspeed greater than V_2 and a climb gradient greater than 2.4% for a twin-engine configuration, 2.7% for a tri-engine configuration, and 3.0% for a quad-engine configuration with one engine inoperative. This climb gradient is of great importance to a high-lift system, because it governs the necessary efficiency of the device. The climb angle is a function of the lift-to-drag ratio for an aircraft with a specified thrust loading:

$$\sin \gamma = \frac{T}{W} - \frac{1}{L/D} \quad (6)$$

Therefore, an aircraft's climb performance can be improved with a high-lift system having a high lift-to-drag ratio. However, this presents a problem in the design of the overall system, for the first and second segments in climb require opposing capabilities.

The high usable lift and maximum lift requirements of the first climb segment demand the use of a leading-edge device, more flap elements, and/or higher flap

deflection angles. This tends to degrade the climb performance needed during the second segment due to a decrease in the lift-to-drag ratio. Consequently, it is important to have the capability to accurately analyze the trade-offs between various high-lift configurations in order to optimize the aerodynamic performance of an aircraft so that it satisfies the FAR Part 25 requirements for both takeoff and landing.

3.2 Landing

The landing performance of a civil transport aircraft consists of an approach, transition from threshold to touchdown, and a braked ground run. The aircraft approaches at a glide slope angle of 3° and must maintain minimum approach and landing speeds as shown in figure 3.2.

The FAR Part 25 requirements specify that the approach speed V_A is at least 1.3 times the minimum dynamic speed V_{MS} or 1.22 times the minimum stall speed $V_{S_{1g}}$ in steady flight. Therefore, a low approach speed necessitates a high maximum lift coefficient; however, the pilot's ground visibility may limit the aircraft's angle of attack during approach. This must be kept in mind during the design phase, because a leading-edge device may push the angle of attack at maximum lift, and consequently the angle of attack at $1.22 \cdot V_{S_{1g}}$, well beyond a safe pitch attitude for visibility. If this occurs, a more complex flap system may be required to shift the lift curve up in order to increase the usable lift coefficient.

Climb gradient is also a factor during the landing maneuver if an aircraft must abort an approach. In general, a lower L/D is desired so that a higher thrust setting can be

used for improved handling and response. However, a climb gradient of 3.2% must be maintained with the flaps deployed, the gear down, and all engines operating if an aircraft has to abort its landing, and as a result a high lift-to-drag ratio is required. Once again trade-offs are necessary, and the high-lift system must be iterated upon to optimize the aircraft's performance.

V_1	$\geq 1.2V_{MCG}$	$\tan \gamma$	≥ 0.024 (twin, engine out)
V_R	$\geq V_1$		≥ 0.027 (tri, engine out)
	$\geq 1.05V_{MC}$		≥ 0.03 (quad, engine out)
V_{LOF}	$\geq 1.1V_{MU}$ (all engines)		
	$\geq 1.05V_{MU}$ (engine out)		
V_2	$\geq 1.13V_{S_{1g}}$		
	$\geq 1.1V_{MC}$		

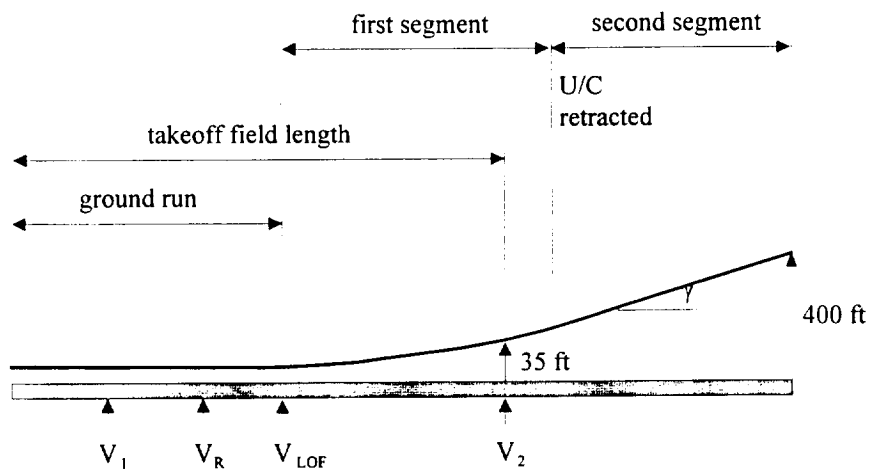


Figure 3.1 FAR 25 Takeoff Requirements

V_A	$\geq 1.22V_{S_{1g}}$
V_{TD}	$\geq 1.08V_{S_{1g}}$

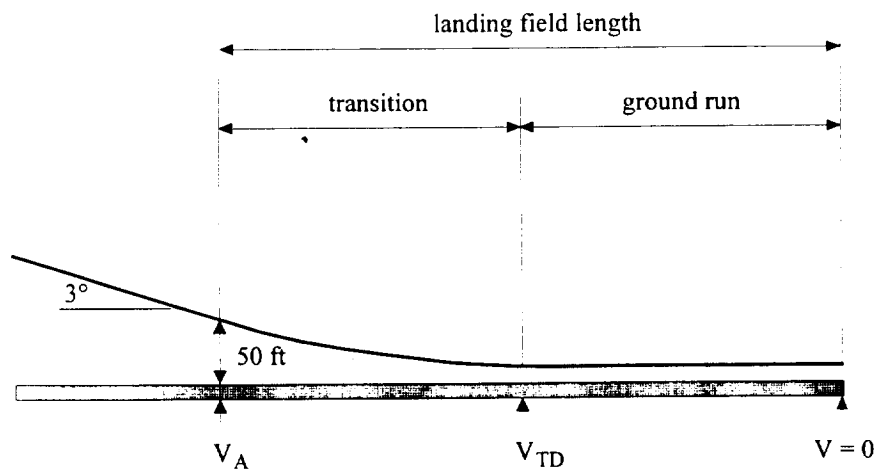


Figure 3.2 FAR 25 Landing Requirements

4.0 Design Constraints

The objective of a high-lift design is to produce the simplest configuration which meets all of the performance requirements. However, this is a difficult job because many limitations hinder the simplicity of the system making its optimization complex.

The wing of a civil transport aircraft is designed to maximize $M \cdot L/D$ for a given payload and mission. Subsequently, the wing area, sweep angle, aspect ratio, twist, and thickness are generally set in the early stages of a preliminary design. One goal of this research is to improve the interaction between the low speed and cruise aerodynamics during the early design phase so that high-lift performance may be considered when designing the wing. This may lead to improved low speed performance, yet the shape of the cruise wing will still impose many restrictions on the design of the high-lift system.

The leading and trailing-edge devices may have constraints placed on their chord, span, or thickness ratio. Given these limitations the designer may have to increase the complexity of the system to comply with performance requirements. For example, if the sweep of the wing degrades the efficiency of a high-lift system to the point where a single-slotted flap is insufficient in producing the required lift, a second flap element may have to be added to increase the effective camber.

The chord length of a slat or flap can be restricted by spar location or internal storage space within the wing. This can happen if a wing suffers from excessive twisting or bending and needs increased structural stiffness. Flap chord can also be limited if an aircraft requires a larger internal fuel volume. In either case, the front or rear spar

location may have to move leaving less room for a high-lift device. In addition, valuable space behind the rear spar may be restricted by landing gear, allowing little room for a retracted flap.

The maximum thickness of a flap element is also a parameter which is often restricted for a designer, because most cruise airfoil shapes are very thin in the trailing-edge region. Although thickness effects of flaps are minimal (especially when employing a leading-edge device), excessively thin flaps can reduce $C_{L_{max}}$ due to flow separation near the leading-edge of the flap. Slender flaps also have a relatively low structural stiffness. Consequently, their panel weight tends to be higher for a given stiffness, and they usually require more supports to maintain optimum gap settings.

Many factors determine the span or continuity of a flap. For instance, inboard ailerons are sometimes necessary for high speed flight, or a thrust gate may be needed because of a short engine mount. This is a very important issue, because nothing is more detrimental to a flap's effectiveness than a discontinuity in its span. A trade-off study should be performed to analyze the effects of engine location on landing gear weight and flap efficiency, since the increase in landing gear weight may be far less than the increase in flap weight if an additional element must be added to the trailing-edge to compensate for a flap cut-out.

One last problem encountered in high-lift system design is that the shape of the leading-edge device is governed by the configuration type. The leading-edge shape of a slat is defined by the cruise wing. This leaves only the shape of the slat cove and the nose of the fixed leading-edge as a design variable. In contrast, a Krüger flap offers versatility in the contour of the leading-edge for optimum performance since it is stowed along the

lower surface of the wing when not in use. Because of this, some argue that a Krüger flap has the potential for a higher L/D and $C_{L_{max}}$.⁷ Nevertheless, a Krüger flap is a very complex device and is generally heavier than a slat. These are the kinds of decisions that are the target of this systematic evaluation algorithm. This research project is intended to develop tools that can be used to better understand the tradeoffs quantitatively so that the optimal configuration may be selected.

5.0 Computational Modeling

Today it is virtually impossible to conduct an extensive experimental program to generate a high-lift database as was done in the United Kingdom during the 1970's and 80's.⁵ However, advances in computational fluid dynamics have made it possible to accurately, yet inexpensively, predict the flow field around multi-element airfoils. Therefore CFD was used as the primary tool in this research project along with some experimental data. The following three viscous-flow solvers for multi-element airfoils were used to generate an aerodynamic database:

1. INS2D^{8,9} This code solves the incompressible Navier-Stokes equations on structured overset meshes. The code was developed by S. Rogers at the NASA Ames Research Center and is widely used in industry for high-lift research.¹⁰
2. NSU2D^{11,12} This code solves the compressible Navier-Stokes equations on unstructured meshes. The code was developed by D. Mavriplis at ICASE and is also widely used in industry.¹³
3. MSES^{14,15} This code solves the Euler equations and integral boundary-layer equations simultaneously. It was developed by M. Drela of MIT and at the high-lift workshop CFD challenge it was shown to be the most accurate viscous/inviscid interaction method.

These three codes are fairly well validated and have been shown to predict changes in the forces and moments due to small differences in a flap configuration.¹⁶ The aerodynamic data obtained with the codes was augmented with experimental data whenever available. The advantage of this hybrid (i.e., computational as well as experimental) approach is that innovative concepts can be analyzed at flight Reynolds

numbers and included in the database much more quickly and inexpensively using CFD than using wind-tunnel experimentation.

Other instances required the use of experimental data because of current CFD limitations. For example, present computational analysis of Krüger flaps is not possible, because the separated flow region behind the flap cannot be modeled accurately. As a result, wind-tunnel data was used to generate the Krüger flap portion of the database.

Special note should also be made that while CFD is able to accurately compute the lift of relatively complex high-lift airfoils, the prediction of drag for these airfoils still remains a challenge. Some engineers argue that the errors involved in predicting drag arise from the inadequacies of the turbulence models used by Navier-Stokes codes. However, this may be only partially true as explained by Vinh et al.¹⁷ They show that even the prediction of drag for multi-element airfoils with attached flow can be inaccurate. They suggest that these errors arise from the method of integration used to calculate the drag force and demonstrate that wake integration techniques provide improved results over surface integration.

6.0 Aerodynamic Database

Computational Fluid Dynamics was used to construct a database consisting of the NLR-7301 two-element and the Douglas LB-546 three-element airfoils. However, the new design methodology is easily extensible, and new systems can be added to the database without difficulty. The two-element and three-element airfoils shown in figure 6.1 were considered because they currently offer high aerodynamic performance. They have also been tested extensively in wind-tunnels and are therefore well documented.

INS2D was used principally to obtain CFD results of the NLR-7301 two-element airfoil. A sample grid of the airfoil used for the calculations is illustrated in figure 6.2. Figure 6.3 shows excellent agreement between INS2D's results and the experimental data¹⁸ for a pressure distribution at an angle of attack of 6° and Reynolds number of 2.51×10^6 . The lift curve for the two-element airfoil can be seen in figure 6.4. The data compares well at low to moderate angles of attack; however, a slight deviation exists at higher angles and at maximum lift. The computational results exhibit an extended stall that continues a few degrees past the wind-tunnel data. This apparent overprediction of $C_{l_{max}}$ has also been encountered by Lin and Dominik.¹⁹ INS2D seems to consistently overestimate the stall angle resulting in a higher value for maximum lift.

Figure 6.5 contains the computed and experimental drag polar of the NLR-7301 airfoil, and again the results show excellent agreement between INS2D and the wind-tunnel data. Also shown in the figure is a drag polar which was fit to the computational data using the RAF parabolic polar estimation method developed by Lean and Fiddes.²⁰

The RAF method was used to construct a drag polar for each high-lift configuration in order to develop the drag prediction method outlined in section 7.1.

INS2D was also used to obtain data of the Douglas three-element airfoil, and an example of a grid used in the computations is illustrated in figure 6.6. Two predicted pressure distributions of the airfoil at an angle of attack of 8.1° and Reynolds number of 9×10^6 are shown in figure 6.7. The difference in the two cases reflects the modeling of the farfield conditions, since grids of the airfoil with and without the wind-tunnel wall were generated to compare with the experimental data. As reported by Kusunose and Cao²¹, including a wind-tunnel wall improved the agreement with the experiment. This is especially evident over the slat, where the case with a wind-tunnel wall did much better in predicting the pressure.

Figures 6.8 and 6.9 illustrate the lift curve and drag polar respectively of the Douglas airfoil. The computational results in these plots represent only the airfoil without wind-tunnel walls, so the results are slightly skewed from the experimental data. Regardless of this discrepancy, the data was used in the construction of the database for this configuration since it more accurately models an airfoil in steady flight.

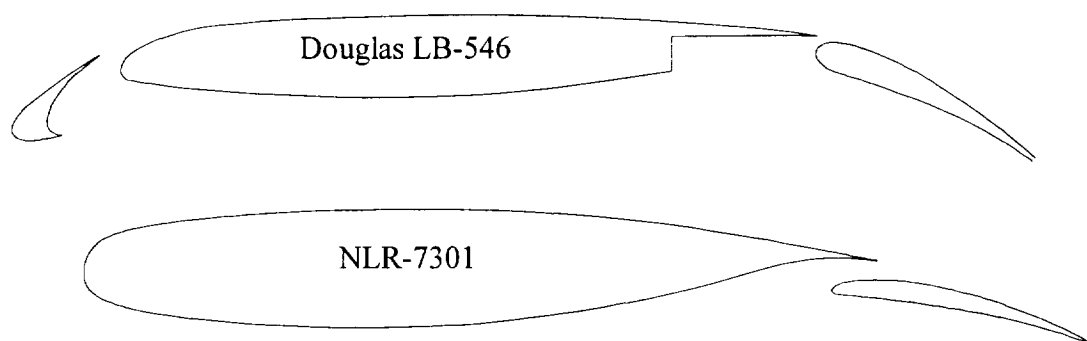


Figure 6.1 Two and Three-Element Airfoil Geometries

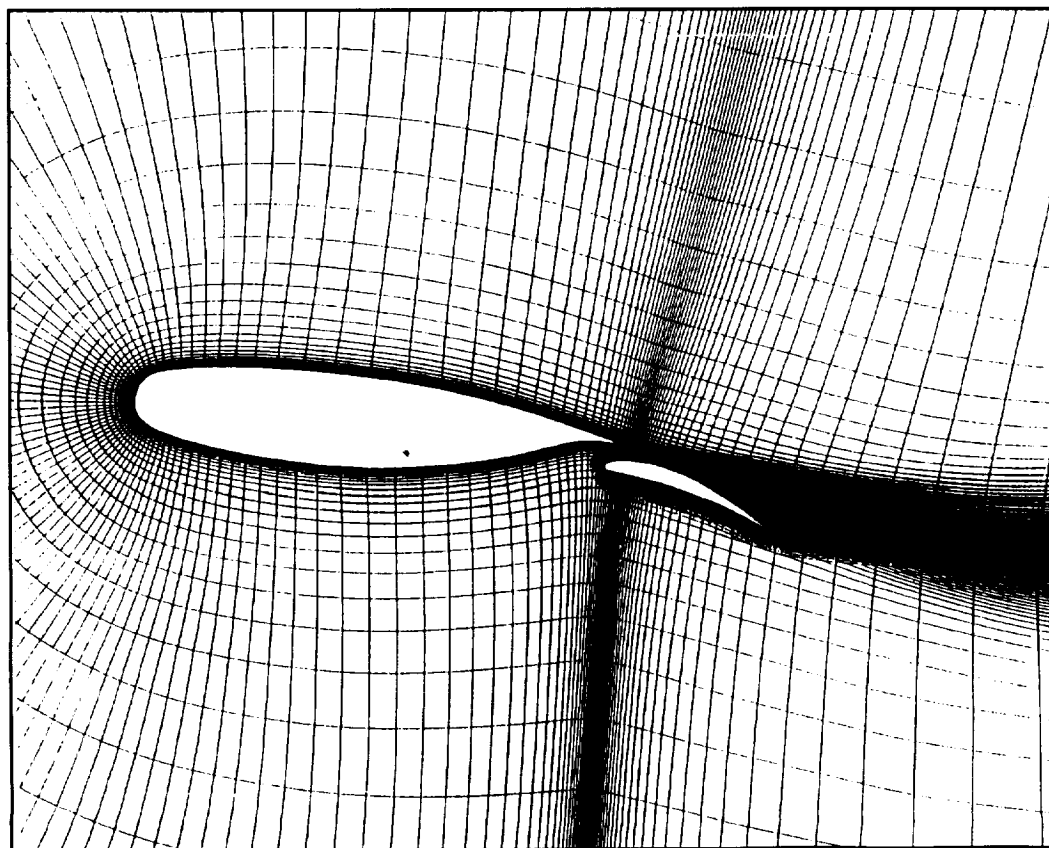


Figure 6.2 Sample CHIMERA Grid of the NLR-7301 Two-Element Airfoil

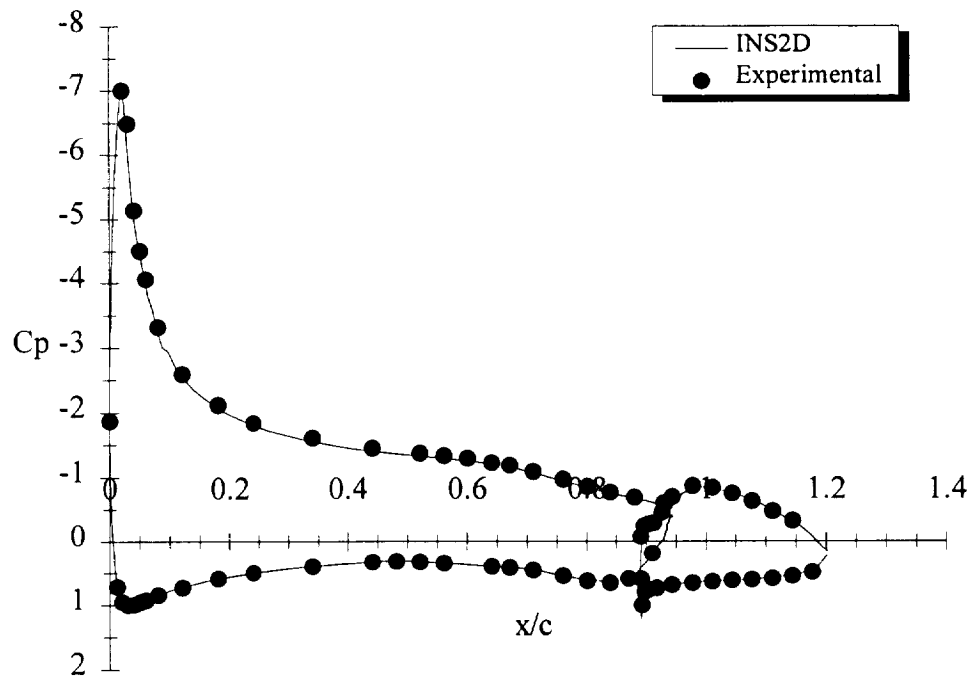


Figure 6.3 NLR-7301 Pressure Distribution ($\alpha=6^\circ$, $Re=2.51 \times 10^6$)

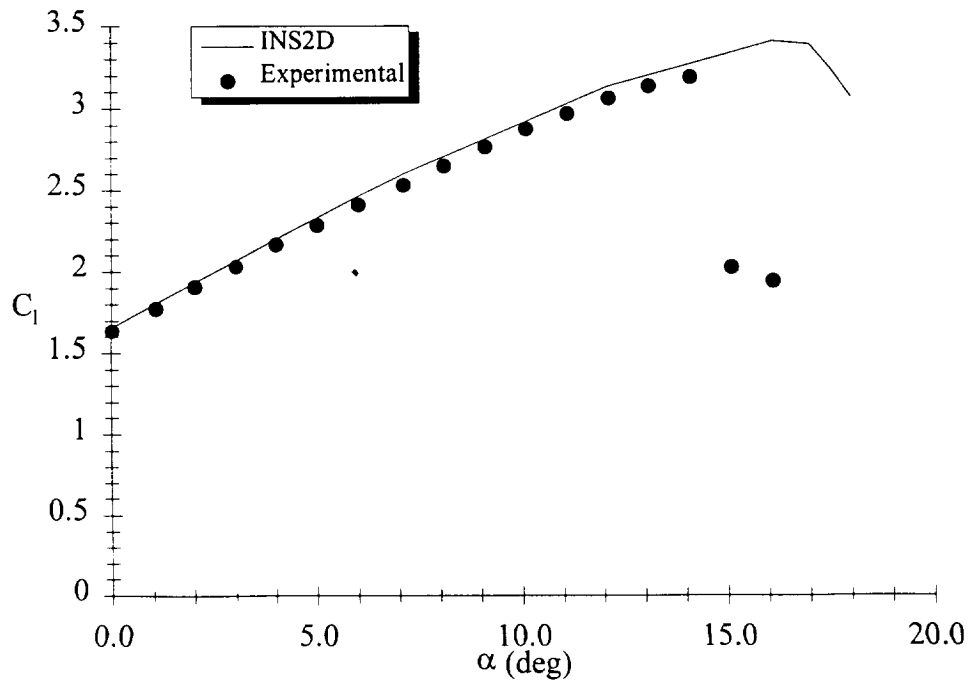


Figure 6.4 NLR-7301 Lift Curve ($Re=2.51 \times 10^6$)

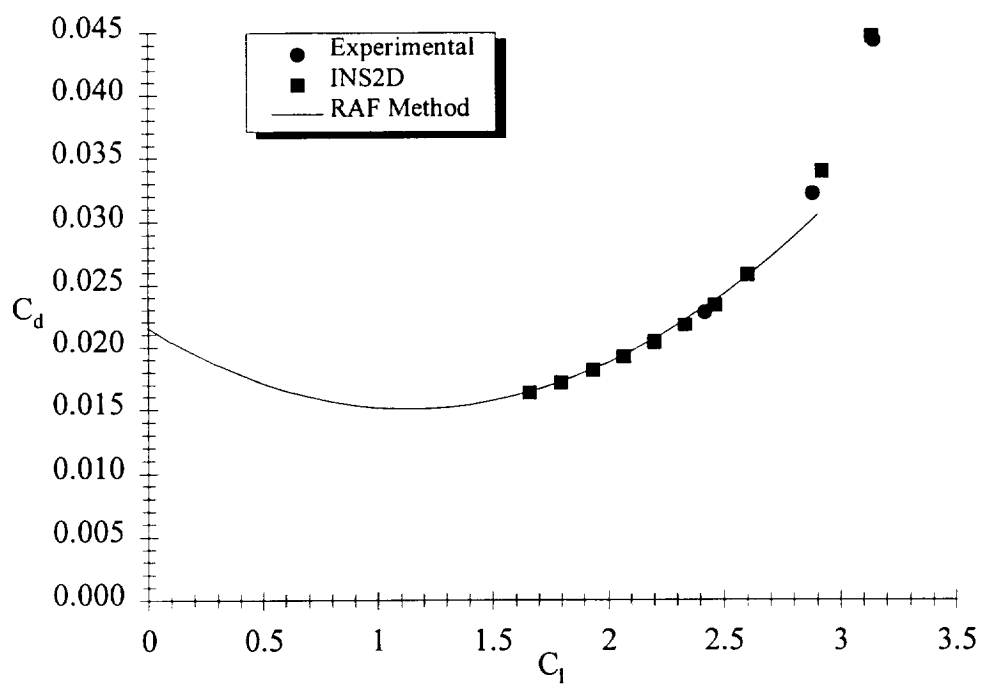


Figure 6.5 NLR-7301 Drag Polar ($Re=2.51 \times 10^6$)

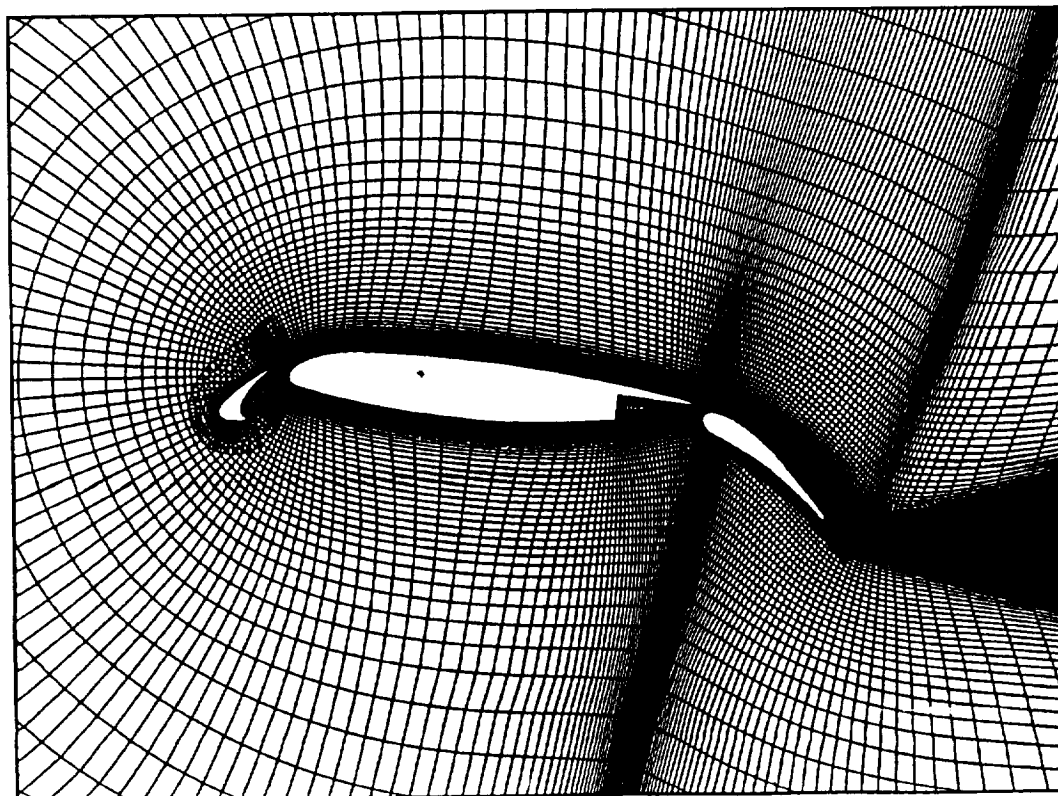


Figure 6.6 Sample CHIMERA Grid of the Douglas LB-546 Three-Element Airfoil

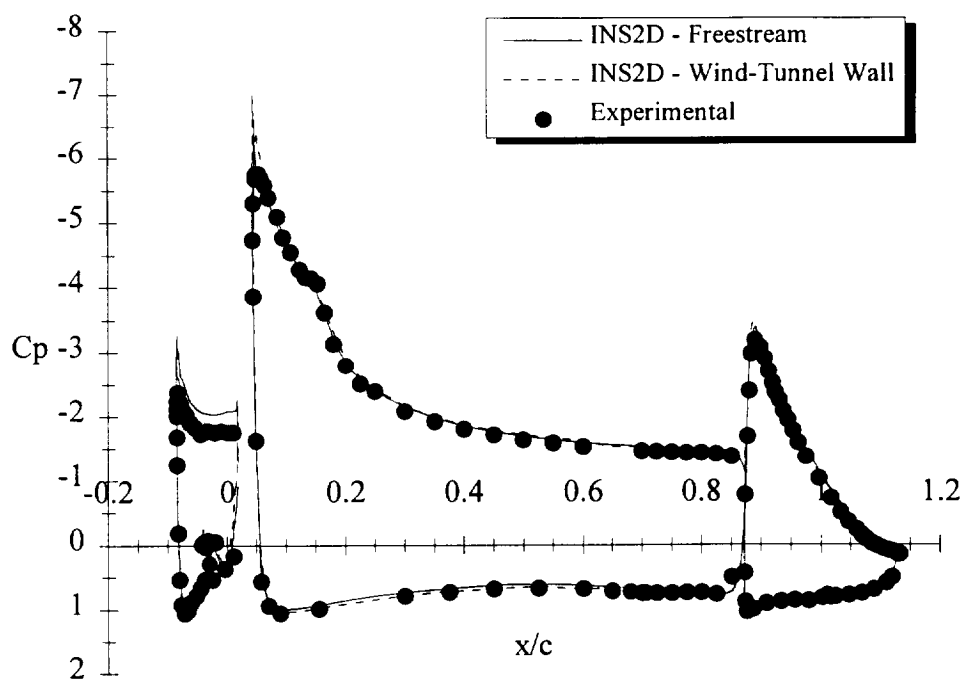


Figure 6.7 Douglas 3-Element Pressure Distribution ($\alpha=8.1^\circ$, $Re=9.0 \times 10^6$)

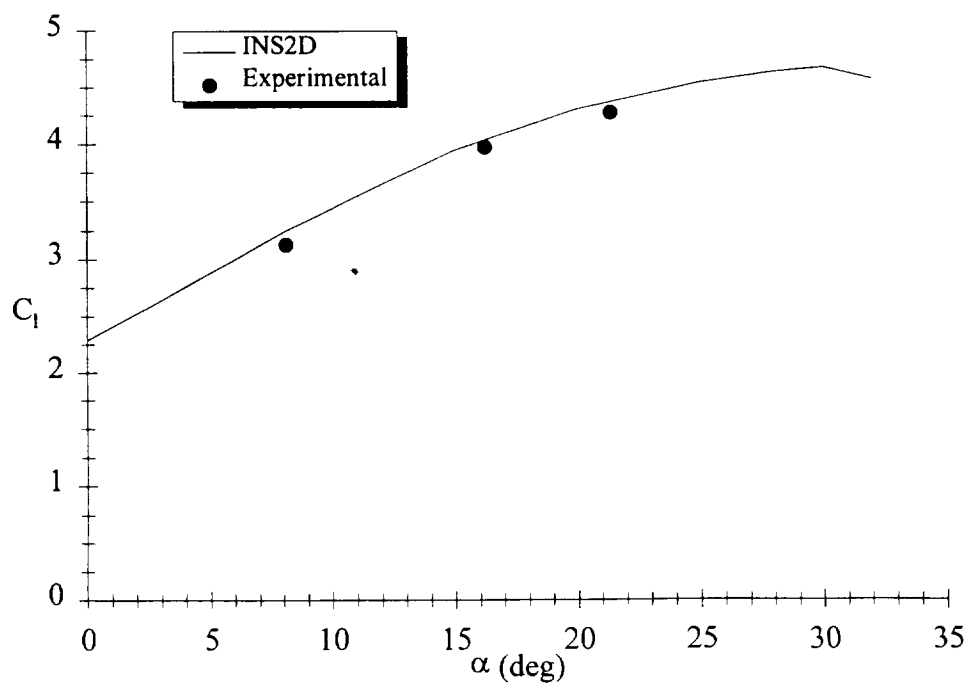


Figure 6.8 Douglas 3-Element Lift Curve ($Re=9.0 \times 10^6$)

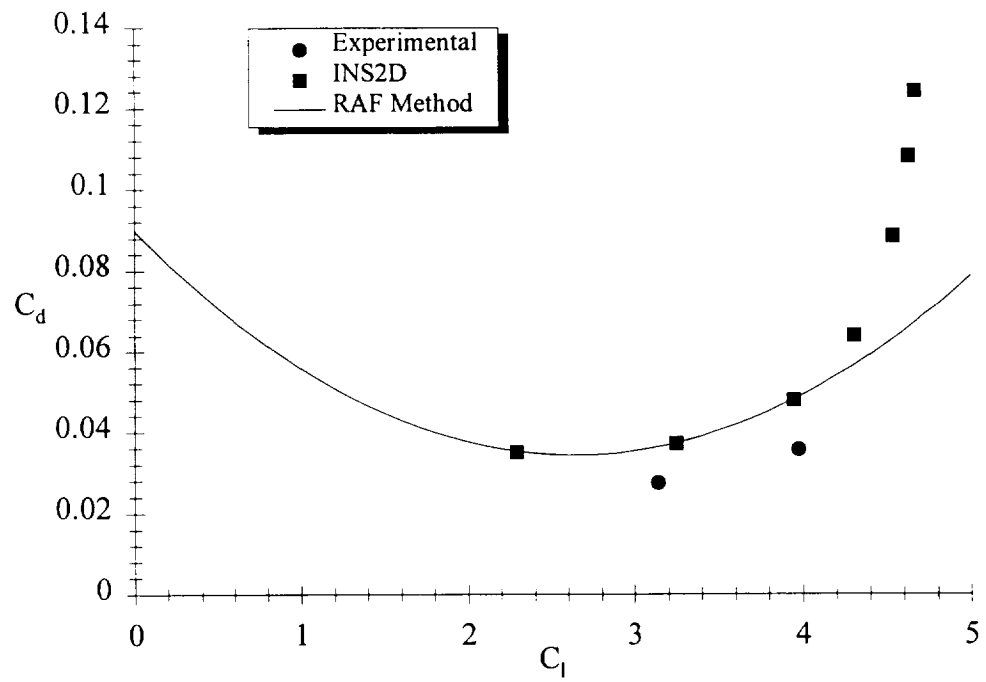


Figure 6.9 Douglas 3-Element Drag Polar ($Re=9.0 \times 10^6$)

7.0 Aerodynamic Module

The newly developed high-lift module predicts the aerodynamic performance for a given high-lift system to be used within a takeoff and landing optimization routine such as ACSYNT. It calculates lift, drag, pitching moment, and maximum lift for a given high-lift system and flight conditions.

The high-lift module first calculates two-dimensional aerodynamic characteristics from equations based on CFD and wind-tunnel data. These aerodynamic characteristics consist of sectional lift curve, profile drag polar, and pitching moment which are calculated from basic airfoil geometry. A modified lifting-line method based on Weissinger's theory²² is then used to determine the total aerodynamic coefficients of the wing. Thus total lift, drag, and pitching moment can be computed faster than with a panel method while incorporating (based on strip theory calculations) the viscous effects of slotted high-lift devices.

7.1 Two-Dimensional Aerodynamics

Theoretical and empirical techniques were applied to develop equations based on the high-lift configuration type, c , t/c , $c_{LE/TE}$, $\delta_{LE/TE}$, α , $\alpha_{o_{clean}}$, C_{l_α} , s_1 , and s_2 from the two-dimensional database in order to calculate α_o , C_{l_α} , $C_{d_{profile}}$, and C_{m_o} .

7.1.1 Lift

A flap is used to produce added lift by increasing the effective camber of an airfoil. Thus, the total lift of an airfoil with extended high-lift devices is represented by the lift of the clean airfoil plus the incremental lift created by the leading and trailing-edge flaps:

$$C_l = C_{l_{\text{clean}}} \frac{c'}{c} + \Delta C_{l_{\text{TE}}} + \Delta C_{l_{\text{LE}}} \quad (7)$$

The lift coefficient for the clean airfoil at a given angle of attack is provided by ACSYNT. The increment in lift coefficient is a function of the flap configuration, geometry, and deflection angle. The additional lift produced by a single-slotted trailing-edge flap is shown below as defined in DATCOM:²³

$$\Delta C_{l_{\text{TE}}} = C_{l_{\alpha_{\text{clean}}}} \alpha_{\delta} \delta_{\text{TE}} \frac{c'}{c} \quad (8)$$

The lift-effectiveness, α_{δ} , is determined for a specified flap configuration type with the general equations shown below:

$$\alpha_{\delta} = -\frac{c_{\text{TE}}}{c} + \chi \left[\alpha_{\delta_{\text{theory}}} f_{t/c} f_{\text{visc}} + \frac{c_{\text{TE}}}{c} \right] \quad (9)$$

$$\alpha_{\delta_{\text{theory}}} = -\frac{2}{\pi} \left[\sqrt{\frac{c_{\text{TE}}}{c} \left(1 - \frac{c_{\text{TE}}}{c} \right)} + \sin^{-1} \sqrt{\frac{c_{\text{TE}}}{c}} \right] \quad (10)$$

$$\chi = \left[1 + a_1 \cdot \tan^{-1} (a_2 \cdot \delta_{\text{TE}}^{x_1}) \right]^{f_{cf}} \quad (11)$$

$$f_{cf} = 1 - b_1 \cdot \frac{c_{\text{TE}}}{c} \quad (12)$$

$$f_{t/c} = 1 + c_1 \cdot t/c \quad (13)$$

$$f_{\text{visc}} = d_1 \quad (14)$$

where a_1 , a_2 , b_1 , c_1 , d_1 , and x_1 are empirical coefficients and were determined to be as follows for both the NLR and Douglas flaps:

$$a_1 = 0.2, \quad a_2 = -5.2, \quad b_1 = 0.55, \quad c_1 = 1.04, \quad d_1 = 0.785, \quad x_1 = 5$$

The expression for the theoretical lift-effectiveness, $\alpha_{\delta_{\text{theory}}}$, is derived for a bent flat plate in an inviscid flow and is a good approximation for small flap deflections.²⁴ It is a function of the flap chord, c_{TE} , only, but an empirical airfoil thickness factor, $f_{t/c}$, and viscous factor, f_{visc} , have been added to account for Reynolds number by scaling $\alpha_{\delta_{\text{theory}}}$ with CFD or experimental data. The separation factor, χ , is used to reduce the lift-effectiveness, α_{δ} , at higher flap deflection angles. The empirical factor is roughly unity at small flap deflections but decreases at larger deflections to account for strong viscous effects and flow separation over the flap. This factor is dependent on the configuration type and the Reynolds number of the CFD or experimental data. Examples of the separation factor and lift-effectiveness curves for the NLR-7301 airfoil are illustrated in figures 7.1 and 7.2 respectively.

It should be noted here that the lift increments of the NLR flap and Douglas flap calculated with this method are both higher than the lift increment of a double-slotted flap calculated via DATCOM.²³ This illustrates the importance of the present methodology, since it is obvious that the performance of current high-lift systems can no longer be predicted with methods that are based on outdated technology and low Reynolds number data.

The primary task of a slat or Krüger flap is to extend the lift curve by increasing the stall angle and as a result increase a wing's maximum lift capability. However, a leading-edge device will slightly alter the lift of a wing. This lift increment is often negligible and may be disregarded in the preliminary design phase, but if the effect is desired, linear theory may be used for a good first approximation. The additional lift produced by a leading-edge device is calculated from:

$$\Delta C_{l_{LE}} = C_{l_{\alpha_{clean}}} \alpha_{\delta_{theory}} \delta_{LE} \frac{c'}{c} \quad (15)$$

where Roshko²⁵ shows that the theoretical lift-effectiveness of a leading-edge device is:

$$\alpha_{\delta_{theory}} = \frac{2}{\pi} \left[\sqrt{\frac{c_{TE}}{c} \left(1 - \frac{c_{TE}}{c} \right)} - \sin^{-1} \sqrt{\frac{c_{TE}}{c}} \right] \quad (16)$$

The extended chord length, c' , is calculated from geometric properties of the leading and trailing-edge devices. This increase in chord is produced by so-called Fowler action and is a very important characteristic of a high-lift device. It can dramatically improve the lift performance of an aircraft without producing excess drag. Examples of Fowler action are shown below for an airfoil with a leading-edge device and a single or double slotted flap.

Single slotted flap:

$$c' = c + f \cdot s_1 + d \cdot c_{LE} \quad (17)$$

The Fowler action functions, f , of the flap and, d , of the slat can be specified by the user, or the default functions may be used. The flap function is based on the assumption that full Fowler motion is reached at a deflection angle of 45° and is specified as:

$$f = \begin{cases} \sin(2\delta_{TE}) & \text{for } \delta_{TE} < 45^\circ \\ 1 & \text{for } \delta_{TE} \geq 45^\circ \end{cases} \quad (18)$$

The leading-edge extension function assumes an increase in Fowler action of 70% of the leading-edge chord for a takeoff position of $\delta_{LE} = 20^\circ$ and 90% for a landing position of $\delta_{LE} = 30^\circ$:

$$d = \sin(2\delta_{LE}^{0.9}) \quad (19)$$

Generally a sealed leading-edge device is employed during takeoff and a vented device is used when landing.

Double slotted flap:

$$c' = c + f_1 \cdot s_1 + f_2 \cdot s_2 + d \cdot c_{LE} \quad (20)$$

The shroud length of the fore flap element is labeled s_2 , and the functions f_1 and f_2 denote the Fowler motion of the vane and the aft flap respectively. These Fowler motion functions shown below specify full fore flap deployment at 45° , beginning deployment of aft flap at 20° , and full aft flap deployment at 50° :

$$f_1 = \begin{cases} \sin(2\delta_{TE}) & \text{for } \delta_{TE} < 45^\circ \\ 1 & \text{for } \delta_{TE} \geq 45^\circ \end{cases} \quad (21)$$

$$f_2 = \begin{cases} 0 & \text{for } \delta_{TE} < 20^\circ \\ \sin[3(\delta_{TE} - 20)] & \text{for } 20^\circ \leq \delta_{TE} < 50^\circ \\ 1 & \text{for } \delta_{TE} \geq 50^\circ \end{cases} \quad (22)$$

The lift curve of the high-lift airfoil can now be determined using the above information. The local lift curve slope for the airfoil is given by:

$$C_{l\alpha} = \chi C_{l\alpha_{\text{clean}}} \frac{c'}{c} \quad (23)$$

Note that the separation factor χ appears once again; this time it accounts for a deviation in the lift curve slope from $2\pi \text{ rad}^{-1}$. Finally, the angle of attack at zero lift for a flapped airfoil can be calculated from:

$$\alpha_o = -\frac{C_{l_o}}{C_{l\alpha}} \quad (24)$$

where the local lift coefficient at zero angle of attack is determined as shown below:

$$C_{l_o} = C_{l_{o_{\text{clean}}}} \frac{c'}{c} + \Delta C_{l_{\text{TE}}} + \Delta C_{l_{\text{LE}}} \quad (25)$$

7.1.2 Drag

A database of minimum drag coefficient, $C_{d_{\text{min}}}$, lift coefficient at minimum drag, $C_{l_{\text{min}}}$, and profile drag constant, k_p , was constructed using the RAF parabolic polar estimation method. Once this database was established, equations for the increments in $C_{d_{\text{min}}}$, $C_{l_{\text{min}}}$, and k_p were determined by fitting curves to the data. The following equations represent the increments associated with a single-slotted trailing-edge flap:

$$\Delta C_{d_{\text{min}_{\text{TE}}}} = a_1 \delta_{\text{TE}}^{x_1} \left(\frac{c_{\text{TE}}}{0.3} \right)^{x_2} \frac{c'}{c} \quad (26)$$

$$\Delta C_{l_{\text{min}_{\text{TE}}}} = \left(b_1 \delta_{\text{TE}} - b_2 \delta_{\text{TE}}^{x_3} \right) \left(\frac{c_{\text{TE}}}{0.3} \right)^{x_4} \frac{c'}{c} \quad (27)$$

$$\Delta k_{p_{\text{TE}}} = \left(c_1 \delta_{\text{TE}} + c_2 \delta_{\text{TE}}^{x_5} \right) \left(\frac{c_{\text{TE}}}{0.3} \right)^{x_5} \frac{c}{c'} \quad (28)$$

where the empirical constants and exponents given below are for both the NLR and Douglas flaps:

$$a_1=0.038, b_1=2.3, b_2=2, c_1=0.00012, c_2=0.0097,$$

$$x_1=1.74, x_2=1.4, x_3=4, x_4=-0.17, x_5=2.55$$

The incremental drag coefficient for a leading-edge flap is extremely dependent on the configuration type, deflection angle, and gap setting. Therefore, no general empirical method for calculating drag increment has been developed. Instead CFD data is used explicitly to give drag increment based on the configuration tested. The Douglas slat is used here to give drag polar information for both the takeoff and landing settings:

Takeoff ($\delta_{LE}=20^\circ$):

$$\Delta C_{d_{min_{LE}}} = 0.0013 \frac{c'}{c} \quad (29)$$

$$\Delta C_{l_{min_{LE}}} = 0.46 \frac{c'}{c} \quad (30)$$

$$\Delta k_{p_{LE}} = 0.00772 \frac{c}{c'} \quad (31)$$

Landing ($\delta_{LE}=30^\circ$):

$$\Delta C_{d_{min_{LE}}} = 0.0074 \frac{c'}{c} \quad (32)$$

$$\Delta C_{l_{min_{LE}}} = 0.76 \frac{c'}{c} \quad (33)$$

$$\Delta k_{p_{LE}} = 0.00381 \frac{c}{c'} \quad (34)$$

The drag polar components of the high-lift airfoil are calculated from the contributions of both the leading and trailing-edge devices and the clean airfoil:

$$C_{d_{\min}} = C_{d_{\min_{\text{clean}}}} \frac{c'}{c} + \Delta C_{d_{\min_{\text{TE}}}} + \Delta C_{d_{\min_{\text{LE}}}} \quad (35)$$

$$C_{l_{\min}} = C_{l_{\min_{\text{clean}}}} \frac{c'}{c} + \Delta C_{l_{\min_{\text{TE}}}} + \Delta C_{l_{\min_{\text{LE}}}} \quad (36)$$

$$k_p = k_{p_{\text{clean}}} \frac{c}{c'} + \Delta k_{p_{\text{TE}}} + \Delta k_{p_{\text{LE}}} \quad (37)$$

These coefficients are then used to construct the following airfoil drag polar which is used to determine profile drag at each section:

$$C_{d_{\text{profile}}} = C_{d_{\min}} + k_p (C_l - C_{l_{\min}})^2 \quad (38)$$

7.1.3 Pitching Moment

The pitching moment about the aerodynamic center (or at zero lift) of the high-lift airfoil is calculated from the pitching moment of the clean airfoil and the contributions from the leading and trailing-edge devices:

$$C_{m_0} = C_{m_{0_{\text{clean}}}} \left(\frac{c'}{c} \right)^2 + \Delta C_{m_{0_{\text{TE}}}} + \Delta C_{m_{0_{\text{LE}}}} \quad (39)$$

The increment in the pitching moment coefficient at the aerodynamic center due to the trailing-edge device is:

$$\Delta C_{m_{0_{\text{TE}}}} = \Delta C_{l_{\text{TE}}} \left(\frac{1}{4} - \frac{x_{cp}}{c'} \frac{c'}{c} \right) \quad (40)$$

The position of the center of pressure, $\frac{x_{cp}}{c'}$, for an airfoil with a single-slotted flap is determined empirically as:

$$\frac{x_{cp}}{c'} = 0.5 - a_1 \delta_{TE}^{x_1} \quad (41)$$

The empirical coefficients a_1 and x_1 were determined to be as follows for both the NLR and Douglas flaps:

$$a_1 = 0.134, \quad x_1 = 0.46$$

The pitching moment increment at the aerodynamic center due to the leading-edge device is:

$$\Delta C_{m_{o_{LE}}} = C_{m_{\delta_{LE}}} \delta_{LE} \left(\frac{c'}{c} \right)^2 \quad (42)$$

where the pitching moment effectiveness about the aerodynamic center is found from thin airfoil theory:²⁶

$$C_{m_{\delta_{LE}}} = -\frac{1}{2} \sin \theta_{LE} (1 - \cos \theta_{LE}) \quad (43)$$

and θ_{LE} is specified as:

$$\theta_{LE} = \cos^{-1} \left(1 - 2 \frac{c_{LE}}{c} \right) \quad (44)$$

The sectional pitching moment about an arbitrary reference point $\frac{x_{ref}}{c}$ is measured from the leading-edge of the clean airfoil is determined as:

$$C_{m_{x_{ref}}} = C_{m_o} + (C_l \cos \alpha + C_d \sin \alpha) \left(\frac{x_{ref}}{c} - \frac{x_{ac}}{c} \right) \quad (45)$$

where C_d includes both the profile drag and induced drag at the section.

The aerodynamic center of the high-lift airfoil is only a function of Fowler action, and its position relative to the leading-edge of the clean airfoil is found by determining the individual shifts in $\frac{x_{ac}}{c}$ due to the leading and trailing-edge devices:

$$\frac{x_{ac}}{c} = \left(\frac{x_{ac}}{c} \right)_{\text{clean}} + \frac{c'}{c} - \left(\frac{c'}{c} \right)_{\text{LE}} \quad (46)$$

where $\left(\frac{c'}{c} \right)_{\text{LE}}$ is the extended chord resulting from only the Fowler action of the leading-edge device.

7.2 Three-Dimensional Aerodynamics

A modified lifting-line method based on Weissinger's theory is applied to determine the spanwise loading across the wing. From this procedure a load distribution can be calculated for a wing of arbitrary planform from sectional lift curve slopes and angles of zero lift. Thus, the total aerodynamic coefficients of the wing can be calculated from a combination of two- and three-dimensional methods. This results in a prediction method which is relatively fast and reflects the viscous nature of slotted flaps.

The Weissinger method accounts for partial span flaps/slats, aspect ratio, and Mach number in order to calculate lift, downwash angle, induced drag, and pitching moment. The geometry of the wing may be asymmetric about the centerline and can include sweep, taper, and twist. The method models the wing as a plate of zero thickness, but the planform and twist remain identical to the actual wing. Thus, partial span flaps

and Fowler action may be modeled as discontinuities in twist and an increase in chord length respectively.

The chordwise load distribution at each span station is concentrated into a lifting line located at the wing's quarter-chord line. The theory requires that the quarter chord line is straight, yet a discontinuity is allowed at the plane of symmetry so that a swept wing may be considered.

The method assumes that the lifting line and its trailing vortex sheet are continuous. However, discrete values for the circulation strength are determined only at the span stations along the quarter-chord line corresponding with control points. The number of control points is specified, and each point is placed at the three-quarter-chord line. Mathematically this implies that the lift curve slope is $2\pi \text{ rad}^{-1}$, so a correction method must be incorporated for a lift curve slope that varies from the theoretical value. For further details please refer to the outline of this correction method in Appendix A.

The general input parameters required by the method are α , AR, $\eta_{LE/TE}$, Λ , λ , M, and S, and the following parameters must be specified at each control point: α_o , C_{l_α} , c, ϵ_w . The chord is defined to be parallel to the freestream direction in the Weissinger method as shown in figure 7.3, so caution should be taken to ensure that all aerodynamic data represent streamwise values. Simple sweep theory dictates that two-dimensional data should be modified from normal (n) to streamwise values as follows:

$$z/c = (z/c)_n \cdot \cos \Lambda \quad (47)$$

$$M = M_n / \cos \Lambda \quad (48)$$

$$Re = Re_n / \cos^2 \Lambda \quad (49)$$

$$C_{l_\alpha} = (C_{l_\alpha})_n \cdot \cos \Lambda \quad (50)$$

$$C_m = (C_m)_n \cdot \cos \Lambda \quad (51)$$

Also, recall that α_o and C_{l_α} were determined previously from sectional CFD and experimental data and are based on the appropriate Reynolds number.

7.2.1 Lift

The Weissinger method determines the local lift coefficient, C_l , at each control point along the wing. From this load distribution the total lift coefficient of the wing, C_L , is determined. The method also returns values for the total lift coefficient of a wing at zero angle of attack, C_{L_0} , the lift curve slope of wing, C_{L_α} , and the downwash angle distribution, ϵ .

Two test cases were used to validate the results of the Weissinger method. Figure 7.4 shows one of these test cases. It is a part-span-flap wing/body configuration with variable twist, and figures 7.5 and 7.6 compare the experimental data²⁷ of this model with predicted load distributions. The other test case is a plain swept wing and is shown in figure 7.7. Similarly, figures 7.8 and 7.9 compare the experimental data²⁸ of this configuration with calculated lift distributions. Both validations compare relatively well with the experimental data; however, there is a slight disagreement at the root of the wing. This discrepancy exists because a body was not modeled computationally in either test case, while both of the experimental models were wing/body configurations.

7.2.2 Drag

Total drag is calculated from both profile drag and induced drag contributions. The Weissinger method determines only the induced drag coefficient, C_{D_i} , so further calculations are required to determine the total drag coefficient of the wing.

Two-dimensional drag polar data is used to calculate the total profile drag by integrating local profile drag across the wing:

$$C_{d_{\text{profile}}} = C_{d_{\text{min}}} + k_p (C_l - C_{l_{\text{min}}})^2 \text{ at station } \eta \quad (52)$$

$$C_{D_{\text{profile}}} = \frac{1}{S} \int_{-b/2}^{y_{\text{body}}} C_d c dy + \frac{1}{S} \int_{y_{\text{body}}}^{b/2} C_d c dy \quad (53)$$

where y_{body} represents the y-coordinate of the exposed wing root. For a symmetric wing, this reduces to:

$$C_{D_{\text{profile}}} = \frac{2}{S} \int_{y_{\text{body}}}^{b/2} [C_{d_{\text{min}}} + k_p (C_l - C_{l_{\text{min}}})^2] c dy \quad (54)$$

The total drag coefficient can now be found by summing the profile drag and induced drag coefficients:

$$C_D = C_{D_{\text{profile}}} + C_{D_{\text{induced}}} \quad (55)$$

7.2.3 Pitching Moment

The total pitching moment about a reference line which is normal to the freestream velocity is calculated as:

$$C_{M_{x_{ref}}} = \frac{2}{S} \int_{y_{body}}^{b/2} C_{m_{x_{ref}}} c dy \quad (56)$$

where the local pitching moment is calculated as shown earlier:

$$C_{m_{x_{ref}}} = C_{m_0} + (C_l \cos \alpha + C_d \sin \alpha) \left(\frac{x_{ref}}{c} - \frac{x_{ac}}{c} \right) \quad (57)$$

Here, the position $\frac{x_{ref}}{c}$ corresponds to a point on the reference line as shown in figure

7.10.

7.3 Maximum Lift Prediction

Maximum lift and stall angle are also calculated using both two- and three-dimensional methods. The maximum local lift coefficient at each spanwise station along the wing is calculated from empirical equations generated from the two-dimensional database. Weissinger's theory is then used to determine the onset of stall by finding the critical section. This method is used to predict maximum lift in the preliminary design process, but other more sophisticated methods should be used in subsequent design phases.

One suggested method that can be implemented into the present methodology is the pressure difference rule developed by Valerezo and Chin.²⁹ This method predicts the maximum lift of an airfoil based on the difference in the peak pressure coefficient and the pressure coefficient at the trailing-edge of an airfoil. The pressure difference rule compares chordwise pressure distributions scaled by their corresponding peak pressure coefficients with a prescribed pressure difference at maximum lift to determine the onset of wing stall for a specified Mach and Reynolds number. This correlation has shown remarkable results and has demonstrated that the method works well for both clean and multi-element airfoils alike, assuming the leading element stalls first.

7.3.1 Two-Dimensional

Empirical equations based on CFD and wind-tunnel data are used to calculate maximum lift at each specified wing station. The general input parameters used to calculate maximum lift are: high-lift configuration type, c , t/c , $c_{LE/TE}$, s_1 , s_2 , $\delta_{LE/TE}$, $\eta_{LE/TE}$, Λ , M , and Re .

The maximum local lift coefficient is calculated from the maximum lift of the clean airfoil and the maximum lift contributions from the leading and trailing-edge devices:

$$C_{l_{max}} = C_{l_{max_{clean}}} \frac{c'}{c} + \Delta C_{l_{max_{LE}}} + \Delta C_{l_{max_{TE}}} \quad (58)$$

$C_{l_{max_{clean}}}$ - clean maximum lift coefficient

$\Delta C_{l_{\max_{LE}}}$ - lift coefficient increment due to the leading-edge device

$\Delta C_{l_{\max_{TE}}}$ - lift coefficient increment due to the trailing-edge device

The increment in maximum lift from a leading-edge device results from a shift in the stall angle of the airfoil:

$$\Delta C_{l_{\max_{LE}}} = C_{l_{\alpha}} \Delta \alpha_{\max} \quad (59)$$

$$\Delta \alpha_{\max} = a_1 + a_2 \left(\frac{c_{LE}}{c} \right) + a_3 \left(\frac{c_{LE}}{c} \right)^2 + a_4 \left(\frac{c_{LE}}{c} \right)^3 \quad (60)$$

The shift in stall angle is only a function of configuration type and leading-edge chord length since the maximum lift performance is fairly insensitive to the angle of the leading-edge device if the gap and overhang are properly optimized.^{5, 30} As mentioned earlier, this shift in angle is constant regardless if the trailing-edge flaps are stowed or deployed. Figure 7.11 illustrates $\Delta \alpha_{\max}$, and table 7.1 gives values for the empirical constants a_1 , a_2 , a_3 , and a_4 .

The increase in maximum lift created by trailing-edge flaps is determined using a type of maximum lift-effectiveness parameter, $C_{l_{\delta_{\max}}}$:

$$\Delta C_{l_{\max_{TE}}} = C_{l_{\delta_{\max}}} \delta_{TE} \frac{c'}{c} \quad (61)$$

$$C_{l_{\delta_{\max}}} = (a_1 + a_2 \delta_{TE}^{x_1}) f_{cf} \quad (62)$$

$$f_{cf} = \left(\frac{c_{TE}}{0.3} \right)^{x_2} \quad (63)$$

where the empirical constants used to calculate the increment in maximum lift for single-slotted flaps are:

$$a_1=153.4, a_2=-151.8, x_1=0.018, x_2=0.16$$

7.3.2 Three-Dimensional

Weissinger's theory is applied to determine the lift distribution across the wing, and the maximum lift is predicted using a critical section approach. It is assumed that the onset of stall occurs when one wing section reaches its maximum lift as illustrated in figure 7.12, yet the wing continues to lift past this critical angle of attack as reported by Murillo and McMasters.³¹ The maximum lift of the wing is evaluated as:

$$C_{L_{\max}} = C_L(\alpha_{\text{crit}}) + f(\text{Re}) \quad (64)$$

where $C_L(\alpha_{\text{crit}})$ corresponds to the lift coefficient at the critical angle of attack, and the function $f(\text{Re})$ is Reynolds number dependent and is assumed to be 10% of $C_L(\alpha_{\text{crit}})$ at the present.

The polynomial method for optimization³² is used to find the critical angle of attack since sectional lift curves may be non-linear. The difference between the local lift coefficient and the local maximum lift coefficient is found at each spanwise station from the provided load distribution. The minimum difference, $(C_l - C_{l_{\max}})_{\min}$, is determined, and the objective function is defined as:

$$f(\alpha) = \left| (C_l - C_{l_{\max}})_{\min} \right| \quad (65)$$

The polynomial optimization method is then used to minimize this function in order to determine the critical angle of attack.

	Sealed Slat	Vented Slat	Sealed Krüger	Vented Krüger
a_1	0.0068	0.017	0.0068	0.017
a_2	0.81	1.28	0.81	1.28
a_3	-1.88	-1.35	-0.37	0.32
a_4	-0.38	-5.5	-0.357	-5.3

Table 7.2 Variables Used to Calculate the Maximum Lift-Effectiveness of Leading-Edge Devices

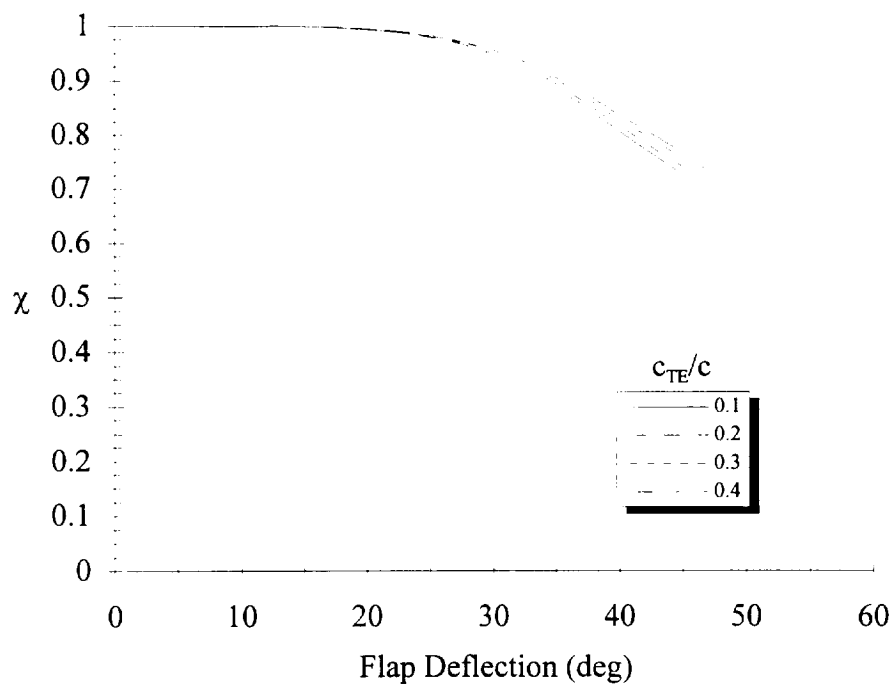


Figure 7.1 NLR-7301 Separation Factor

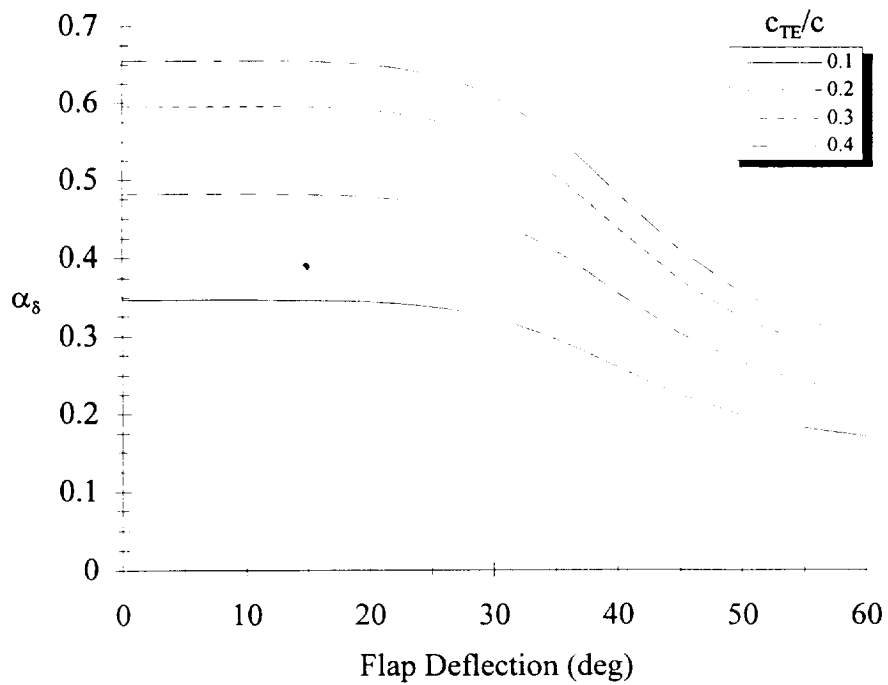
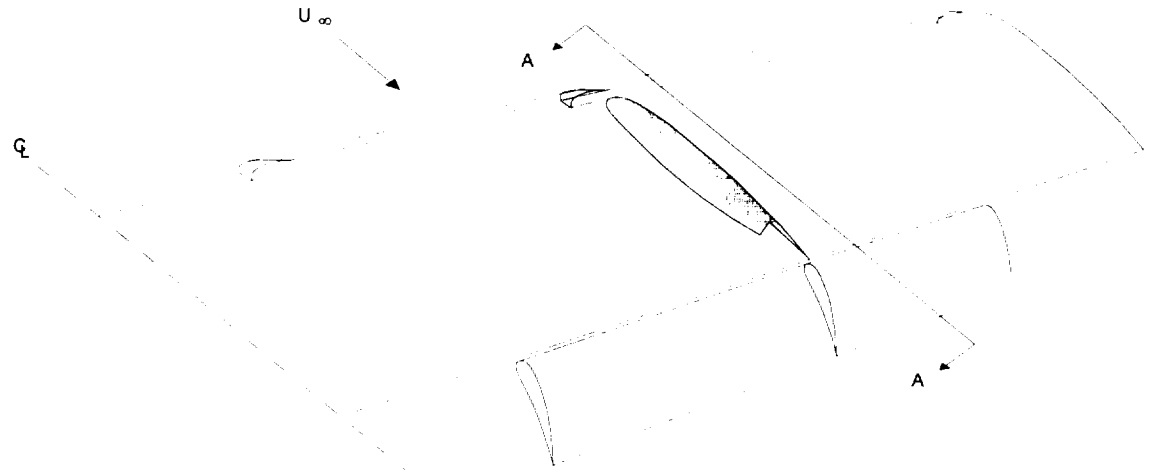


Figure 7.2 NLR-7301 Lift-Effectiveness



2-D
Reynolds Averaged N-S Method

3-D
Modified Lifting-Line Method

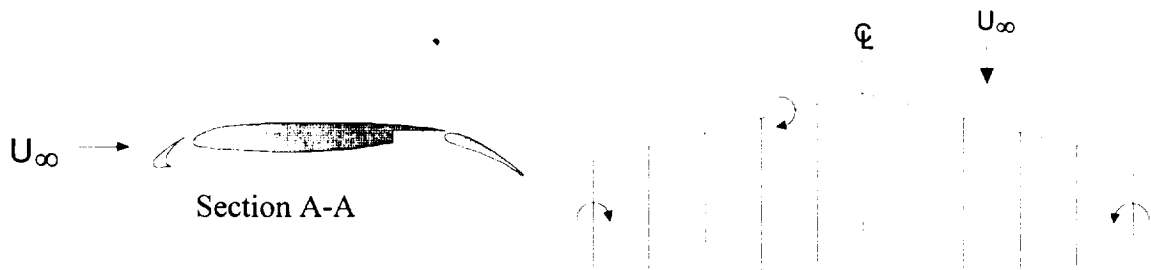


Figure 7.3 Overview of Aerodynamic Analysis

Wind-tunnel measurements using a variable twist wing (VTW) model in the NASA Langley 14- by 22-Foot Tunnel at a Reynolds number of 1×10^6 and lift coefficient of 0.6.

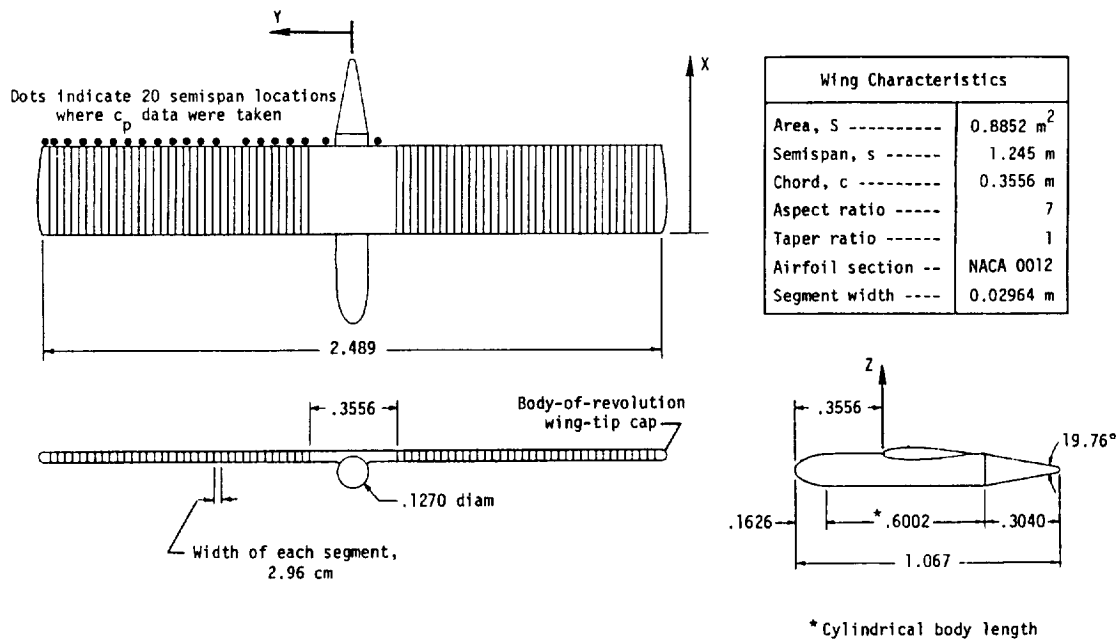


Figure 7.4 Part-Span-Flap Deflection Test Case (from Ref. 27)

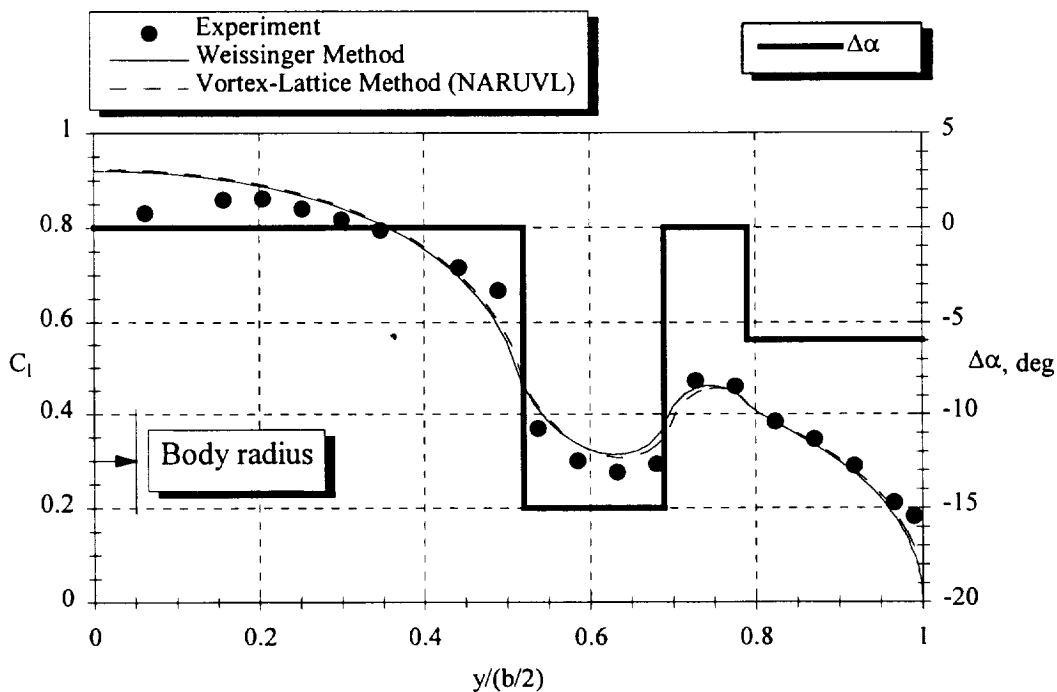


Figure 7.5 Part-Span-Flap Spanwise Load Distribution
VTW7S1 Configuration, $\alpha=11.4^\circ$

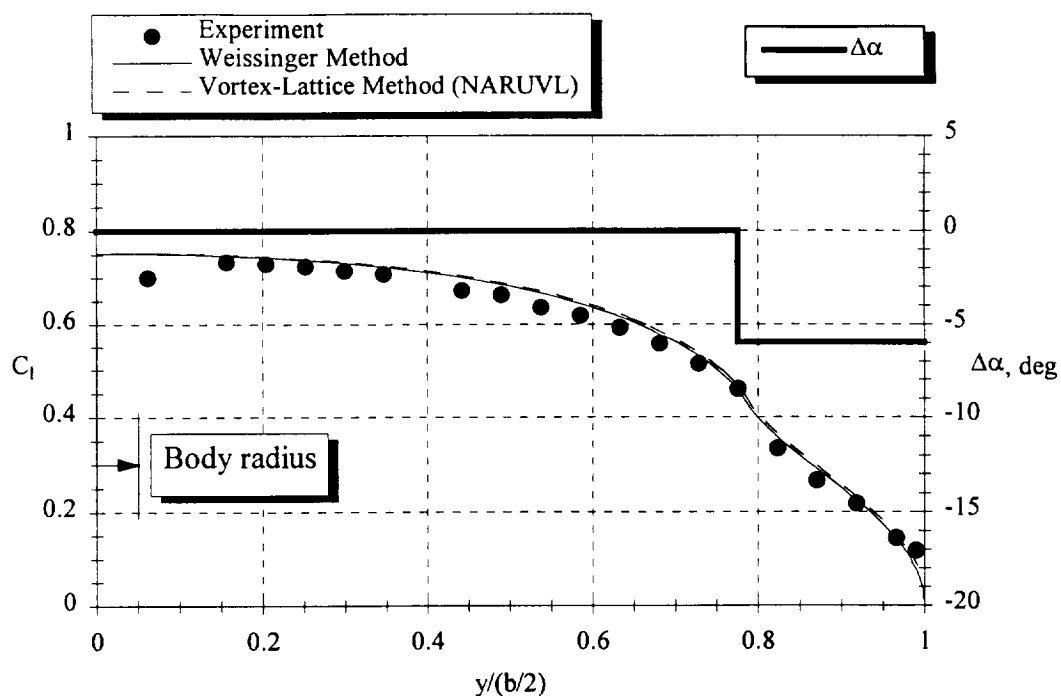


Figure 7.6 Part-Span-Flap Spanwise Load Distribution
VTW7 Configuration, $\alpha=8.5^\circ$

Wind-tunnel measurements using two semispan wing-fuselage models in the NASA Ames 40- by 80-Foot Tunnel at a Reynolds number of 8×10^6 .

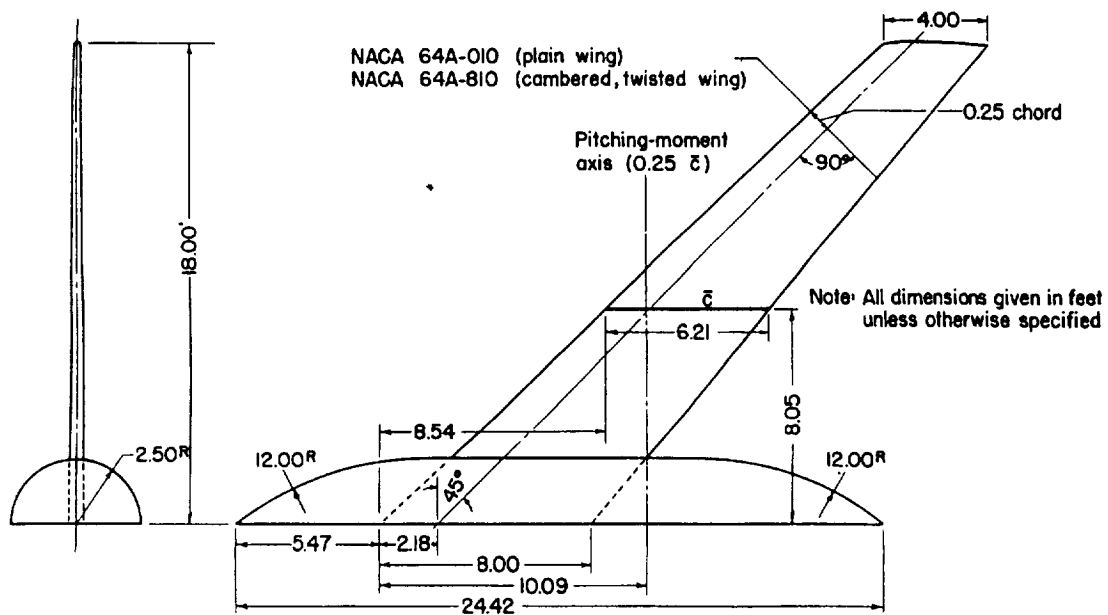


Figure 7.7 Swept-Wing Test Case (from Ref. 28)

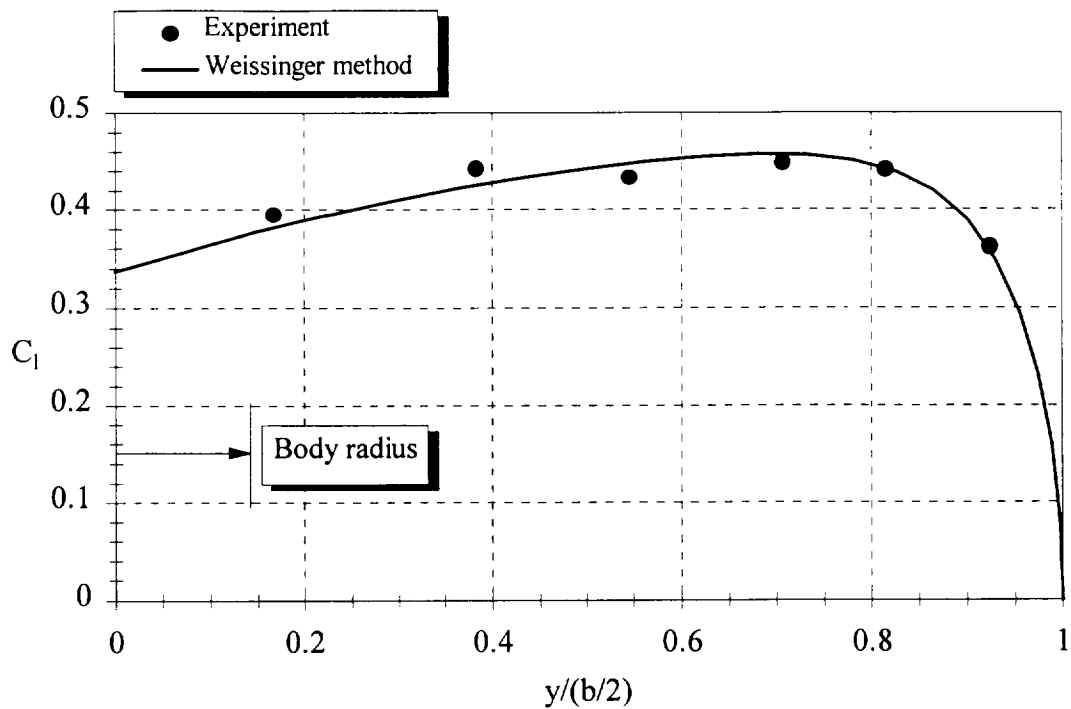


Figure 7.8 Swept-Wing Lift Distribution
Plain Wing Model, $C_L=0.4$

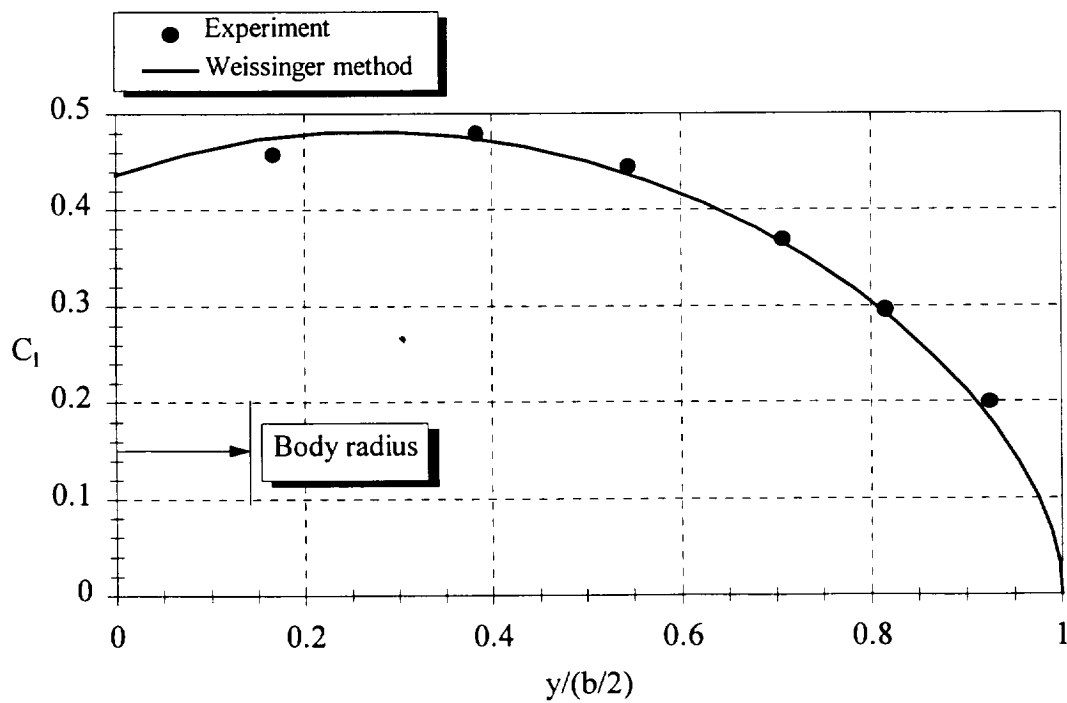


Figure 7.9 Swept-Wing Lift Distribution
Cambered & Twisted Wing Model, $C_L=0.4$

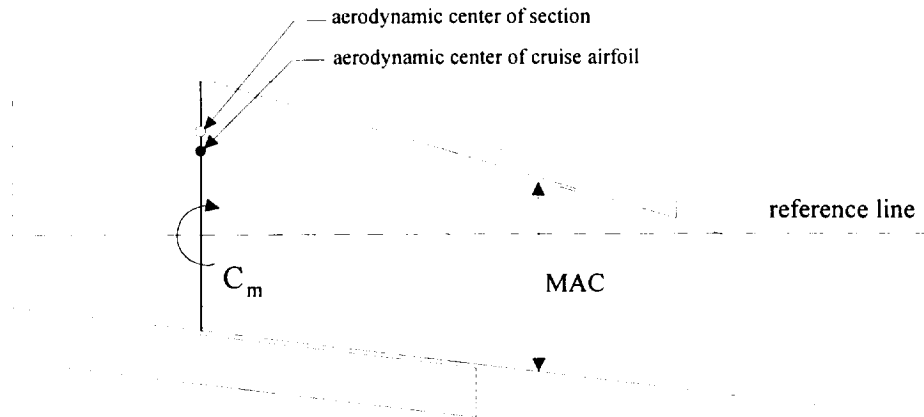


Figure 7.10 Procedure for Calculating Pitching Moment

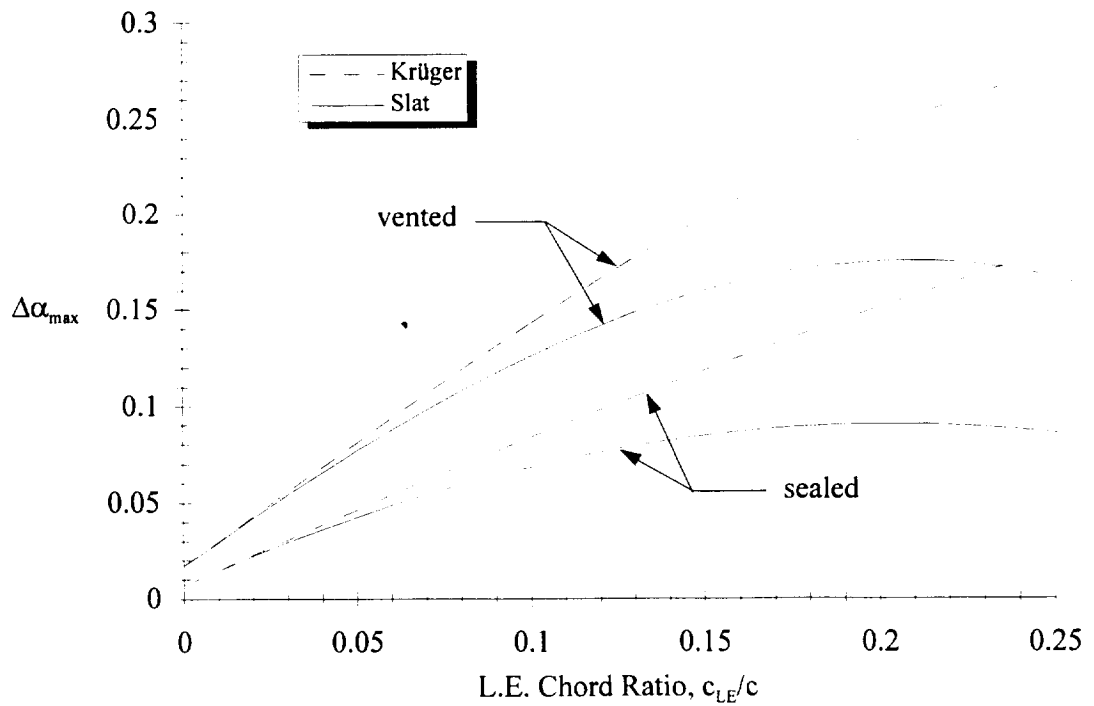


Figure 7.11 Increment In Stall Angle Due to Various L. E. Devices

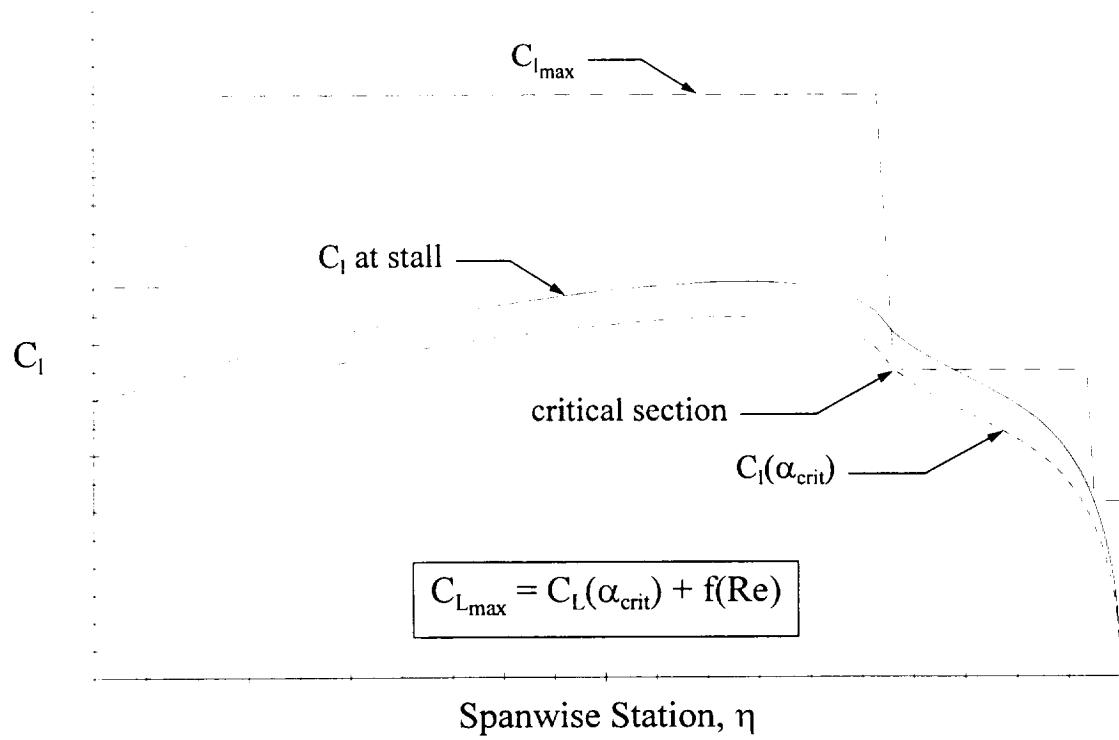


Figure 7.12 Maximum Lift Estimation Using Critical Section Approach

8.0 Weight Module

The weight of the high-lift system is an important factor in the preliminary design phase of an aircraft. The system weight is very much governed by the aerodynamic loads, the structural materials, and the structural stiffness requirements. Other important factors that may affect the overall weight of the high-lift system are fail-safe design requirements, system complexity, and system reliability. However, it is important to note that information on the weight and the aerodynamic performance of a high-lift device is not sufficient to determine the optimal system. The optimal system depends on the effects of the high-lift system on the weight and cost of the complete aircraft. For instance, a variable camber Krüger flap may be heavier than a slat; yet, as a result of a slightly higher maximum lift, it may produce a substantial increase in maximum payload for a given aircraft geometry and mission profile.

This estimation method was developed to offer a parametric weight sensitivity analysis for weight and cost trade-off studies. It uses empirical equations based on historic data to calculate incremental weights due to leading and trailing-edge devices. The method predicts leading and trailing-edge surface, support, support fairing, actuation, and fixed structure weights for a given high-lift system. As a result, changes in the technology of materials, geometry, mechanisms, or actuation can be reflected through the scaling of the various weight components.

The equations are based solely on stowed flap area, so they require minimal geometric data to evaluate system weight in the preliminary design phase. This

represents a reduction in complexity from existing weight estimation methods such as those by Anderson et al.³³ and Oman.³⁴ These methods, which are based on numerous high-lift parameters, are very difficult to correlate with the limited data that is available, and they often result in trends that are not realistic. Thus, a simpler approach was adopted to construct a fast, robust, and fairly accurate weight prediction method for multi-element wings.

8.1 Trailing-Edge Flap Weight

Flap panel, support structure, support fairing, and actuation weight correlations are shown below. These weights are based on stowed flap area for a given flap configuration and support type. The specific weights a_1 , a_2 , a_3 , and a_4 are given in tables 8.1 - 8.3. Trailing-edge weight correlations are shown for several aircraft in figure 8.1.

Surface Structure:

$$W_{\text{panel}} = a_1 \cdot S_{\text{TE}} \quad (66)$$

Support Structure:

$$W_{\text{support}} = a_2 \cdot f_{\text{fow}} \cdot S_{\text{TE}} \quad (67)$$

$$f_{\text{fow}} = \begin{cases} 0.47 + 0.53 \frac{R_{\text{fow}}}{0.5} & \text{for linkage and external hinge supports} \\ 1 & \text{for track supports} \end{cases} \quad (68)$$

$$R_{fow} = \frac{\Delta S_{Fowler}}{S_{TE}} \quad (69)$$

where f_{fow} is a function of Fowler motion and is used to scale the weights of linkage and externally hinged supports and fairings. The term R_{fow} is the ratio of Fowler area to the area of the trailing-edge flap.

Support Fairing:

$$W_{fairing} = a_3 \cdot f_{fow} \cdot S_{TE} \quad (70)$$

Actuation:

$$W_{actuation} = a_4 \cdot S_{TE} \quad (71)$$

Total Trailing-Edge Flap Weight:

$$W_{TE} = W_{panel} + W_{support} + W_{fairing} + W_{actuation} \quad (72)$$

The fixed trailing-edge weight of the wing is also determined in order to calculate the total wing weight. This weight is estimated using the equation developed by Anderson et al.:³⁵

$$W_{fixedTE} = 1.34 \left(S_{fixedTE} \right)^{1.089} \geq 2.0 \cdot S_{fixedTE} \quad (73)$$

where $S_{fixedTE}$ is the area of the fixed trailing-edge and is calculated as:

$$S_{fixedTE} = S_{TEgross} - \left(S_{TE} + S_{ail} + 0.5 \cdot S_{sp} \right) \quad (74)$$

The gross trailing-edge area of the wing is represented by $S_{TE_{gross}}$, and the aileron and spoiler areas are denoted as S_{ail} and S_{sp} , respectively.

8.2 Leading-Edge Flap Weight

As with the trailing-edge flaps, the leading-edge device component weights are based on nested flap area as shown below. The specific weights a_5 , a_6 , and a_7 are given in table 8.4, and correlations for leading-edge weights of several airplanes are plotted in figure 8.2.

Moving Panels:

$$W_{moving} = a_5 \cdot S_{LE} \quad (75)$$

Actuation:

$$W_{actuation} = a_6 \cdot S_{LE} \quad (76)$$

Fixed Leading-Edge:

$$W_{fixed} = a_7 \cdot S_{LE} \quad (77)$$

Total Leading-Edge Flap Weight:

$$W_{LE} = W_{moving} + W_{actuation} + W_{fixed} \quad (78)$$

The above methods for predicting leading-edge device, trailing-edge device, and fixed trailing-edge weight along with the methods for estimating aileron and spoiler weight (shown in Appendix B) will be used in conjunction with the wing box weight estimation method developed by Ardema et al.³⁶ to determine the total weight of the wing within ACSYNT.

This prediction method is intended to be used only in the preliminary design phase of an aircraft. However, the methodology lends itself to an improved weight estimation method for subsequent design phases, since experimental data shows³⁷ that flap loading is independent of angle of attack and is only a function of flap deflection. The proposed idea involves changing the routine from a 0th order to a 1st order predictive method so that CFD results can be used in conjunction with slender beam analysis to determine the weight of a configuration. Thus, the chordwise load distribution supplied by CFD and the spanwise load distribution provided by the Weissinger method can be used to determine the weight of a high-lift system for a given flap placard speed (maximum speed allowed with flaps deployed) with a specified support type and number of supports.

Once this method is developed, the loading information provided by CFD can also be used as an input in the calculation of wing box weight. This will provide valuable information for calculating the torsional loads produced by the flaps. Consequently, the structural analysis of the wing box will include information regarding the flap configuration and Fowler action.

Specific Weight	Single-Slotted	Fixed Vane/Main	Articulating Vane/Main	Main/Aft	Triple-Slotted
Flap Panel (a_1)	2.7	3	3.5	4.8	5.5
Support (a_2)	3.0	3.2	3.8	4.7	5.6
Fairing (a_3)	1.0	1.0	1.15	1.3	1.4
Actuation (a_4)	2.2	2.2	2.3	2.4	2.5
Total	8.9	9.4	10.75	13.2	15

Table 8.1 Specific Weights of Trailing-Edge Flaps with Hooked Track Supports
(lb / ft² of stowed flap area)

Specific Weight	Single-Slotted	Fixed Vane/Main	Articulating Vane/Main	Main/Aft	Triple-Slotted
Flap Panel (a_1)	2.7	3.0	3.5	4.8	5.5
Support (a_2)	1.5	1.6	1.9	2.4	2.8
Fairing (a_3)	0.11	0.11	0.13	0.14	0.16
Actuation (a_4)	2.0	2.0	2.1	2.2	2.3
Total	6.31	6.71	7.63	9.54	10.76

Table 8.2 Specific Weights of Trailing-Edge Flaps with Link/Track Supports
(lb / ft² of stowed flap area)

Specific Weight	Single-Slotted	Fixed Vane/Main	Articulating Vane/Main	Main/Aft
Flap Panel (a_1)	2.7	3.0	3.5	4.8
Support (a_2)	1.1	1.2	1.8	2.2
Fairing (a_3)	0.28	0.28	0.29	0.29
Actuation (a_4)	0.9	1.0	1.3	1.5
Total	4.98	5.48	6.89	8.79

Table 8.3 Specific Weights of Trailing-Edge Flaps with External Hinge Supports
(lb / ft² of stowed flap area)

Flap Type	Fixed Camber Krüger	Variable Camber Krüger	Slat without Slave Tracks	Slat with Slave Tracks
Movable L. E. (a_5)	4	5.1	7.7	8.5
Actuation (a_6)	2.8	2.8	2.1	2.1
Fixed L. E. (a_7)	6	8.5	4.5	4.7
Total	12.8	16.4	14.3	15.3

Table 8.4 Specific Weights of Leading-Edge Devices
(lb / ft² of stowed flap area)

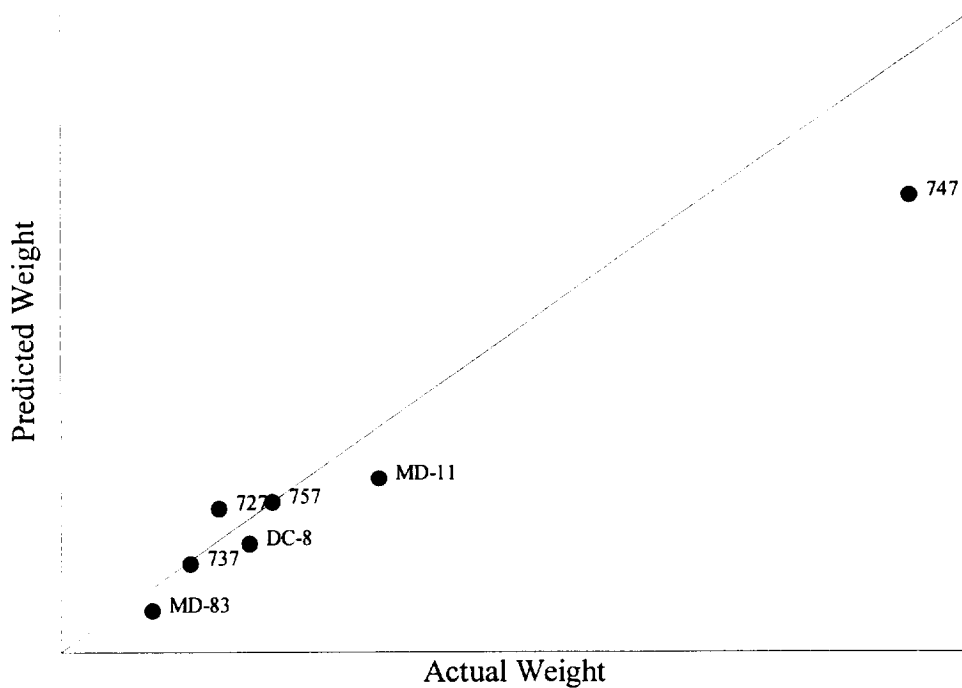


Figure 8.1 Trailing-Edge Weight Correlations for Various Aircraft

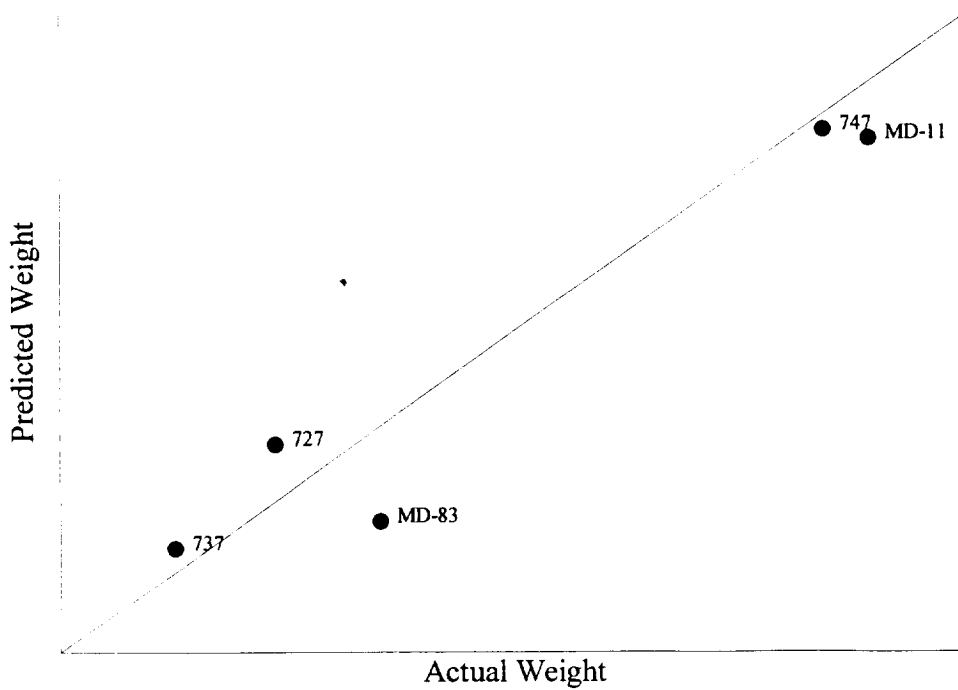


Figure 8.2 Leading-Edge Weight Correlations for Various Aircraft

9.0 Cost Module

The impact that a high-lift system has on the total life cycle cost of a transport aircraft is a complex function of the costs to develop, build, purchase, operate, maintain and dispose of the airplane. As described by Gelhausen³⁸, the total cost of the system is best captured in the direct operating cost (DOC) where the costs to own and operate the aircraft are combined. The DOC includes fuel, airframe, crew, and maintenance expenses and is the most important parameter used when comparing civil transport aircraft with equivalent missions. A full mission and market analysis is required to show the effects of improved high-lift system performance. This includes improved fuel economy, the increase in range and payload, and the increase in units sold. However, the cost to manufacture and maintain the system must be analyzed in order to understand the complete picture. For instance, a system that is more complex but generates a higher maximum lift may result in improved cruise efficiency and reduced fuel expenditures, but at the same time may cause increased airframe and maintenance cost. It is important to not only provide the aerodynamic and weight information, but also the cost information to the synthesis process. This methodology incorporates system cost so that careful tradeoff studies can be conducted to determine the optimal high-lift system for a new aircraft.

The system cost is governed by the weight, W , and the part count, PC of the high-lift device:³⁹

$$\text{Cost} = a_1 \cdot W \cdot PC^{x_1} \quad (79)$$

$$a_1 = \begin{cases} 1.8881 & \text{trailing - edge device} \\ 1.7339 & \text{leading - edge device} \end{cases}$$

$$x_1 = 0.7$$

Here the constant, a_1 , accounts for hourly labor costs and type of material. Historically, weight has been the most important parameter, but recently more information regarding part count has also become available. For instance, Boeing simplified the flap system on the new 737 from a triple-slotted to a double-slotted design. The new flap system has 37% fewer parts and 33% fewer bearings.⁴⁰ This reduction in part affects cost (note, however, that the reduction in cost is reported to be significantly less than 30% indicating a value for the part count exponent, x_1 , significantly less than unity) and, consequently, the newly developed cost module incorporates this factor as well as system weight.

The total part count of a system is found by summing up the various components of the device. The part count of a trailing-edge flap consists of the flap panel, support, support fairing, and actuation:

$$PC_{TE} = PC_{\text{panel}} + PC_{\text{support}} + PC_{\text{fairing}} + PC_{\text{actuation}} \quad (80)$$

The part count of a leading-edge device is the sum of the movable leading-edge, actuation, and fixed leading-edge:

$$PC_{LE} = PC_{\text{movable}} + PC_{\text{actuation}} + PC_{\text{fixed}} \quad (81)$$

Each category is a function of the flap configuration and support type only. The total part count is used as a measure of overall system “complexity”, while the size of the device and complexity associated with Fowler action are reflected in the weight of the flap.

Values for part count components of trailing-edge devices are given in tables 9.1 - 9.3, and component values for leading-edge devices are given in table 9.4.

Part Count Component	Single-Slotted	Fixed Vane/Main	Articulating Vane/Main	Main/Aft	Triple-Slotted
Flap Panel	600	750	820	1400	1620
Support	210	210	230	230	260
Fairing	350	360	370	380	500
Actuation	450	450	450	450	450
Total	1610	1770	1870	2460	2830

Table 9.1 Part Count of Trailing-Edge Flaps with Hooked Track Supports

Part Count Component	Single-Slotted	Fixed Vane/Main	Articulating Vane/Main	Main/Aft	Triple-Slotted
Flap Panel	600	750	820	1400	1620
Support	150	150	164	164	185
Fairing	100	100	105	110	145
Actuation	300	300	300	300	300
Total	1150	1300	1389	1974	2250

Table 9.2 Part Count of Trailing-Edge Flaps with Link/Track Supports

Part Count Component	Single-Slotted	Fixed Vane/Main	Articulating Vane/Main	Main/Aft
Flap Panel	590	740	810	1380
Support	200	200	220	220
Fairing	200	205	210	220
Actuation	200	200	200	200
Total	1190	1345	1440	2020

Table 9.3 Part Count of Trailing-Edge Flaps with External Hinge Supports

Part Count Component	Slat with Slave Tracks	Slat without Slave Tracks	Fixed Camber Krüger	Variable Camber Krüger
Movable L. E.	1000	840	800	1500
Actuation	300	300	300	400
Fixed L. E.	1400	1100	1000	1200
Total	2700	2240	2100	3100

Table 9.4 Part Count of Leading-Edge Devices

10.0 Sample Application

The design methodology previously described was applied to evaluate a high-lift configuration on a DC-9 type wing. The basic geometry of this test case consists of a 1,000 ft² wing with an aspect ratio of 8.5, taper ratio of 0.25, wash-out of 3°, and a quarter-chord sweep angle of 24°. The wing thickness varies from 13% at the root to 10% at the tip. The high-lift system consists of a full span slat with a chord of 0.15c and a single-slotted flap with hooked track supports, a chord of 0.36c, and a semi-span of 0.67 b/2. The aerodynamic performance of the wing with extended trailing-edge flaps is evaluated with the slat both retracted and deployed, and system weight and cost are determined for both leading and trailing-devices.

Given:

$$S = 1,000 \text{ ft}^2$$

$$AR = 8.5$$

$$\lambda = 0.25$$

$$\varepsilon_w = 3.0^\circ$$

$$\Lambda = 24^\circ$$

$$\frac{S_1}{c} = 0.08$$

$$\frac{c_{TE}}{c} = 0.36$$

$$\frac{c_{LE}}{c} = 0.145$$

$$\eta_{TE_{inb'd}} = 0.10$$

$$\eta_{TE_{outb'd}} = 0.77$$

$$\eta_{LE_{inb'd}} = 0.10$$

$$\eta_{LE_{outb'd}} = 0.97$$

$$\delta_{TE} = 30^\circ = 0.524 \text{ rad}$$

$$\delta_{LE} = 30^\circ = 0.524 \text{ rad}$$

Assume for simplicity that the aerodynamic characteristics of the cruise airfoil sections remain constant along the span:

$$C_{l_{\alpha_{\text{clean}}}} = 5.49 \text{ rad}^{-1}$$

$$C_{l_{o_{\text{clean}}}} = 0.225$$

$$C_{d_{\text{min}_{\text{clean}}}} = 0.0067$$

$$C_{l_{\text{min}_{\text{clean}}}} = 0.225$$

$$k_{p_{\text{clean}}} = 0.0038$$

$$C_{l_{\text{max}_{\text{clean}}}} = 1.575$$

$$C_{m_{o_{\text{clean}}}} = -0.06$$

$$\left(\frac{dC_m}{dC_l} \right)_{\text{clean}} = -0.039$$

Airfoil with extended trailing-edge flap only

Calculate lift curve slope using the default Fowler motion function:

$$f = \sin[2(0.524)] = 0.866 \quad \text{from eqtn. (18)}$$

$$\frac{c'}{c} = 1 + 0.08(0.866) = 1.07 \quad \text{from eqtn. (17)}$$

$$f_{cf} = 1 - 0.55(0.36) = 0.802 \quad \text{from eqtn. (12)}$$

$$\chi = \left\{ 1 + 0.2 \tan^{-1} \left[\frac{5.2(0.524)^5}{f} \right] \right\}^{0.802} = 0.967 \quad \text{from eqtn. (11)}$$

$$C_{l_{\alpha}} = 0.967(5.49)(1.07) = 5.680 \text{ rad}^{-1} \quad \text{from eqtn. (23)}$$

Next, the angle of attack at zero lift is calculated at the flap panel edges for example, but α_o should be calculated at each control point along the wing in order to determine the spanwise lift distribution:

$$\alpha_{\delta_{\text{theory}}} = -\frac{2}{\pi} \left[\sqrt{0.36(1-0.36)} + \sin^{-1} \sqrt{0.36} \right] = 0.715 \quad \text{from eqtn. (10)}$$

$$f_{\text{visc}} = 0.785 \quad \text{from eqtn. (14)}$$

at inboard section of flap panel, $\eta_{\text{TEinb'd}} = 0.10$:

$$t/c = 0.13$$

$$f_{t/c} = 1 + 1.04(0.13) = 1.135 \quad \text{from eqtn. (13)}$$

$$\alpha_{\delta} = -0.36 + 0.967[(0.715)(1.135)(0.785) + 0.36] = 0.604 \quad \text{from eqtn. (9)}$$

$$\Delta C_{l_{\text{TE}}} = 5.49(0.604)(0.524)(1.07) = 1.859 \quad \text{from eqtn. (8)}$$

$$C_{l_o} = 0.225(1.07) + 1.859 = 2.100 \quad \text{from eqtn. (25)}$$

$$\alpha_o = -\frac{2.100}{5.680} = -0.370 \text{ rad} \quad \text{from eqtn. (24)}$$

at outboard section of flap panel, $\eta_{\text{TEoutb'd}} = 0.77$:

$$\begin{aligned} t/c &= t/c_{\text{root}} - \frac{\eta_{\text{TEoutb'd}} - \eta_{\text{root}}}{1 - \eta_{\text{root}}} (t/c_{\text{root}} - t/c_{\text{tip}}) \\ &= 0.13 - \frac{0.77 - 0.10}{1 - 0.10} (0.13 - 0.10) = 0.108 \end{aligned}$$

$$f_{t/c} = 1 + 1.04(0.108) = 1.112 \quad \text{from eqtn. (13)}$$

$$\alpha_{\delta} = -0.36 + 0.967[(0.715)(1.112)(0.785) + 0.36] = 0.592 \quad \text{from eqtn. (9)}$$

$$\Delta C_{l_{\text{TE}}} = 5.49(0.592)(0.524)(1.07) = 1.822 \quad \text{from eqtn. (8)}$$

$$C_{l_o} = 0.225(1.07) + 1.822 = 2.063 \quad \text{from eqtn. (25)}$$

$$\alpha_o = -\frac{2.063}{5.680} = -0.363 \text{ rad} \quad \text{from eqtn. (24)}$$

Calculate drag polar:

$$\begin{aligned}\Delta C_{d_{\min TE}} &= 0.038(0.524)^{1.74} \left(\frac{0.36}{0.3}\right)^{1.4} (1.07) && \text{from eqtn. (26)} \\ &= 0.0170\end{aligned}$$

$$\begin{aligned}\Delta C_{l_{\min TE}} &= \left[2.3(0.524) - 2(0.524)^4\right] \left(\frac{0.36}{0.3}\right)^{-0.17} (1.07) && \text{from eqtn. (27)} \\ &= 1.09\end{aligned}$$

$$\begin{aligned}\Delta k_p &= \left[0.00012(0.524) + 0.0097(0.524)^2\right] \left(\frac{0.36}{0.3}\right)^{2.55} \left(\frac{1}{1.07}\right) && \text{from eqtn. (28)} \\ &= 0.00406\end{aligned}$$

$$C_{d_{\min}} = 0.0067(1.07) + 0.0170 = 0.0242 \quad \text{from eqtn. (35)}$$

$$C_{l_{\min}} = 0.225(1.07) + 1.09 = 1.33 \quad \text{from eqtn. (36)}$$

$$k_p = 0.0038 \left(\frac{1}{1.07}\right) + 0.00406 = 0.00761 \quad \text{from eqtn. (37)}$$

$$C_{d_{\text{profile}}} = 0.0242 + 0.00761(C_l - 1.33)^2 \quad \text{from eqtn. (38)}$$

Calculate pitching moment about the aerodynamic center:

$$\frac{x_{cp}}{c'} = 0.5 - 0.134(0.524)^{0.46} = 0.400 \quad \text{from eqtn. (41)}$$

at inboard section of flap panel:

$$\Delta C_{m_{TE}} = 1.859[0.25 - 0.400(1.07)] = -0.331 \quad \text{from eqtn. (40)}$$

$$C_{m_o} = -0.06(1.07)^2 - 0.331 = -0.400 \quad \text{from eqtn. (39)}$$

at outboard section of flap panel:

$$\Delta C_{m_{TE}} = 1.822[0.25 - 0.400(1.07)] = -0.324 \quad \text{from eqtn. (40)}$$

$$C_{m_0} = -0.06(1.07)^2 - 0.324 = -0.393 \quad \text{from eqtn. (39)}$$

C_{l_α} and α_0 are given as input to the Weissinger method in order to calculate the lift distribution of the wing. The lift distribution can now be used to calculate C_L , C_{D_i} , $C_{D_{\text{profile}}}$, and C_M . The total aerodynamic coefficients of the wing are given in table 10.1.

Calculate maximum sectional lift:

$$f_{cf} = \left(\frac{0.36}{0.3} \right)^{0.16} = 1.030 \quad \text{from eqtn. (63)}$$

$$C_{l_{\delta_{\text{max}}}} = \left[8.8 - 7.8(0.524)^{0.65} \right] (1.030) = 3.786 \quad \text{from eqtn. (62)}$$

$$\Delta C_{l_{\text{max}_{TE}}} = 3.786(0.524)(1.07) = 2.123 \quad \text{from eqtn. (61)}$$

$$C_{l_{\text{max}}} = 1.575(1.07) + 2.123 = 3.81 \quad \text{from eqtn. (58)}$$

Airfoil with extended trailing-edge flap and slat

Calculate lift curve slope using the default Fowler motion function:

$$f = \sin[2(0.524)] = 0.866 \quad \text{from eqtn. (18)}$$

$$d = \sin[2(0.524)^{0.9}] = 0.899 \quad \text{from eqtn. (19)}$$

$$\frac{c'}{c} = 1 + 0.866(0.08) + 0.899(0.145) = 1.20 \quad \text{from eqtn. (17)}$$

f_{c_f} and χ do not change with the addition of a leading-edge device.

$$C_{l_\alpha} = 0.967(5.49)(1.20) = 6.371 \text{ rad}^{-1} \quad \text{from eqtn. (23)}$$

Calculate the angle of attack at zero lift at the flap panel edges:

The lift-effectiveness of the flap remains the same with the addition of a slat.

at inboard section of flap panel, $\eta_{TE_{inb'd}} = 0.10$:

$$\Delta C_{l_{TE}} = 5.49(0.604)(0.524)(1.20) = 2.085 \quad \text{from eqtn. (8)}$$

$$C_{l_o} = 0.225(1.20) + 2.085 = 2.355 \quad \text{from eqtn. (25)}$$

$$\alpha_o = -\frac{2.355}{6.371} = -0.370 \text{ rad} \quad \text{from eqtn. (24)}$$

at outboard section of flap panel, $\eta_{TE_{outb'd}} = 0.77$:

$$\Delta C_{l_{TE}} = 5.49(0.592)(0.524)(1.20) = 2.044 \quad \text{from eqtn. (8)}$$

$$C_{l_o} = 0.225(1.20) + 2.044 = 2.314 \quad \text{from eqtn. (25)}$$

$$\alpha_o = -\frac{2.314}{6.371} = -0.363 \text{ rad} \quad \text{from eqtn. (24)}$$

Calculate drag polar:

$$\Delta C_{d_{minTE}} = 0.038(0.524)^{1.74} \left(\frac{0.36}{0.3} \right)^{1.4} (1.20) = 0.0191 \quad \text{from eqtn. (26)}$$

$$\begin{aligned} \Delta C_{l_{minTE}} &= \left[2.3(0.524) - 2(0.524)^4 \right] \left(\frac{0.36}{0.3} \right)^{-0.17} (1.20) \quad \text{from eqtn. (27)} \\ &= 1.23 \end{aligned}$$

$$\begin{aligned} \Delta k_{p_{TE}} &= \left[0.00012(0.524) + 0.0097(0.524)^2 \right] \left(\frac{0.36}{0.3} \right)^{2.55} \left(\frac{1}{1.20} \right) \quad \text{from eqtn. (28)} \\ &= 0.00362 \end{aligned}$$

$$\Delta C_{d_{\min LE}} = 0.0074(1.20) = 0.0089 \quad \text{from eqtn. (32)}$$

$$\Delta C_{l_{\min TE}} = 0.76(1.20) = 0.91 \quad \text{from eqtn. (33)}$$

$$\Delta k_{p_{LE}} = 0.00381 \left(\frac{1}{1.20} \right) = 0.00318 \quad \text{from eqtn. (34)}$$

$$C_{d_{\min}} = 0.0067(1.20) + 0.0191 + 0.0089 = 0.0360 \quad \text{from eqtn. (35)}$$

$$C_{l_{\min}} = 0.225(1.20) + 1.23 + 0.91 = 2.41 \quad \text{from eqtn. (36)}$$

$$k_p = 0.0038 \left(\frac{1}{1.20} \right) + 0.00362 + 0.00318 = 0.00997 \quad \text{from eqtn. (37)}$$

$$C_{d_{\text{profile}}} = 0.0360 + 0.00997(C_1 - 2.41)^2 \quad \text{from eqtn. (38)}$$

Calculate pitching moment about the aerodynamic center:

$$\frac{x_{cp}}{c'} = 0.400 \quad \text{from eqtn. (41)}$$

$$\theta_{LE} = \cos^{-1}[1 - 2(0.145)] = 0.781 \text{ rad} \quad \text{from eqtn. (44)}$$

$$C_{m_{\delta LE}} = -\frac{1}{2} \sin(0.781)[1 - \cos(0.781)] = -0.102 \text{ rad}^{-1} \quad \text{from eqtn. (43)}$$

$$\Delta C_{m_{o_{LE}}} = -0.102(0.524)(1.20)^2 = -0.0770 \quad \text{from eqtn. (42)}$$

at inboard section of flap panel:

$$\Delta C_{m_{TE}} = 2.085[0.25 - 0.400(1.20)] = -0.480 \quad \text{from eqtn. (40)}$$

$$C_{m_o} = -0.06(1.20)^2 - 0.480 - 0.0770 = -0.643 \quad \text{from eqtn. (39)}$$

at outboard section of flap panel:

$$\Delta C_{m_{TE}} = 2.044[0.25 - 0.400(1.20)] = -0.470 \quad \text{from eqtn. (40)}$$

$$C_{m_o} = -0.06(1.20)^2 - 0.470 - 0.0770 = -0.633 \quad \text{from eqtn. (39)}$$

Calculate maximum sectional lift:

$$\Delta C_{l_{max_{TE}}} = 3.786(0.524)(1.20) = 2.381 \quad \text{from eqtn. (61)}$$

$$\begin{aligned} \Delta \alpha_{max} &= 0.023 + 1.7(0.145) - 1.8(0.145)^2 - 7.3(0.145)^3 \\ &= 0.209 \end{aligned} \quad \text{from eqtn. (60)}$$

$$\Delta C_{l_{max_{LE}}} = 6.371(0.209) = 1.332 \quad \text{from eqtn. (59)}$$

$$C_{l_{max}} = 1.575(1.20) + 2.381 + 1.332 = 5.60 \quad \text{from eqtn. (58)}$$

This information is insufficient to determine the optimum high-lift system, so the weight and cost data is calculated next.

Calculate weight and cost of trailing-edge flap:

$$\begin{aligned} c_{TE_{inb'd}} &= 0.36c_{inb'd} \\ &= 0.36c_{root} \\ &= 0.36 \frac{2 \cdot \sqrt{S}}{1 + \lambda \sqrt{AR}} \\ &= 0.36 \frac{2}{1 + 0.25} \sqrt{\frac{1000}{8.5}} \\ &= 6.248 \text{ ft} \end{aligned}$$

$$\begin{aligned}
c_{TE_{outb'd}} &= 0.36c_{outb'd} \\
&= 0.36c_{root} \left[1 - \frac{\eta_{TE_{outb'd}} - \eta_{root}}{1 - \eta_{root}} (1 - \lambda) \right] \\
&= 0.36 \frac{2}{1 + \lambda} \sqrt{\frac{S}{AR}} \left[1 - \frac{\eta_{TE_{outb'd}} - \eta_{root}}{1 - \eta_{root}} (1 - \lambda) \right] \\
&= 0.36 \frac{2}{1 + 0.25} \sqrt{\frac{1000}{8.5}} \left[1 - \frac{0.77 - 0.1}{1 - 0.1} (1 - 0.25) \right] \\
&= 2.759 \text{ ft}
\end{aligned}$$

$$\begin{aligned}
S_{TE} &= (c_{TE_{inb'd}} + c_{TE_{outb'd}}) \eta_{TE} \frac{b}{2} \\
&= (c_{TE_{inb'd}} + c_{TE_{outb'd}}) \eta_{TE} \frac{\sqrt{S \cdot AR}}{2} \\
&= (6.248 + 2.759) 0.67 \frac{\sqrt{1000(8.5)}}{2} \\
&= 278.2 \text{ ft}^2
\end{aligned}$$

Since $f_{row}=1$, equation (72) reduces to:

$$W_{TE} = (a_1 + a_2 + a_3 + a_4) S_{TE}$$

$$W_{TE} = 8.9(278.2) = 2476 \text{ lb}$$

$$PC_{TE} = 1610$$

from eqn. (80)

$$\text{Cost}_{TE} = 1.8881(2476)(1610)^{0.7} = \$ 0.821 \times 10^6$$

from eqn. (79)

Calculate weight and cost of slat:

$$\begin{aligned}
c_{LE_{inb'd}} &= 0.145c_{inb'd} = 0.145c_{root} \\
&= 0.145 \frac{2}{1 + \lambda} \sqrt{\frac{S}{AR}} \\
&= 0.145 \frac{2}{1 + 0.25} \sqrt{\frac{1000}{8.5}} \\
&= 2.516 \text{ ft}
\end{aligned}$$

$$\begin{aligned}
c_{LE_{outb'd}} &= 0.145c_{outb'd} \\
&= 0.145c_{root} \left[1 - \frac{\eta_{LE_{outb'd}} - \eta_{root}}{1 - \eta_{root}} (1 - \lambda) \right] \\
&= 0.145 \frac{2}{1 + \lambda} \sqrt{\frac{S}{AR}} \left[1 - \frac{\eta_{LE_{outb'd}} - \eta_{root}}{1 - \eta_{root}} (1 - \lambda) \right] \\
&= 0.145 \frac{2}{1 + 0.25} \sqrt{\frac{1000}{8.5}} \left[1 - \frac{0.97 - 0.1}{1 - 0.1} (1 - 0.25) \right] \\
&= 0.692 \text{ ft}
\end{aligned}$$

$$\begin{aligned}
S_{LE} &= (c_{LE_{inb'd}} + c_{LE_{outb'd}}) \eta_{LE} \frac{b}{2} \\
&= (c_{LE_{inb'd}} + c_{LE_{outb'd}}) \eta_{LE} \frac{\sqrt{S \cdot AR}}{2} \\
&= (2.516 + 0.692) 0.87 \frac{\sqrt{1000(8.5)}}{2} \\
&= 128.7 \text{ ft}^2
\end{aligned}$$

Equation (78) can be expressed as:

$$W_{LE} = (a_5 + a_6 + a_7) S_{LE}$$

$$W_{LE} = 15.3(128.7) = 1969 \text{ lb}$$

$$PC_{LE} = 3100 \quad \text{from eqtn. (81)}$$

$$\text{Cost}_{LE} = 1.7339(1969)(3100)^{0.7} = \$ 0.949 \times 10^6 \quad \text{from eqtn. (79)}$$

A summary of the results is shown in tables 10.1 and 10.2 and figures 10.1 and 10.2

	Single-Slotted	Single-Slotted with 3 Position Slat
C_{L_0}	1.28	1.38
$C_D (\alpha=0^\circ)$	0.0953	0.1228
$C_{L_{max}}$	1.95	3.03
α_{max} , deg	9.32	21.1

Table 10.1 Aerodynamic Performance of a Single-Slotted Flap With a Track Support (With and Without a Slat)

	Single-Slotted	3 Position Slat	Total
System Weight, lb	2476	1969	4445
System Cost, \$	0.821×10^6	0.949×10^6	1.770×10^6

Table 10.2 System Weight and Cost Data of a Single-Slotted Flap With a Track Support and a Slat With Slave Tracks

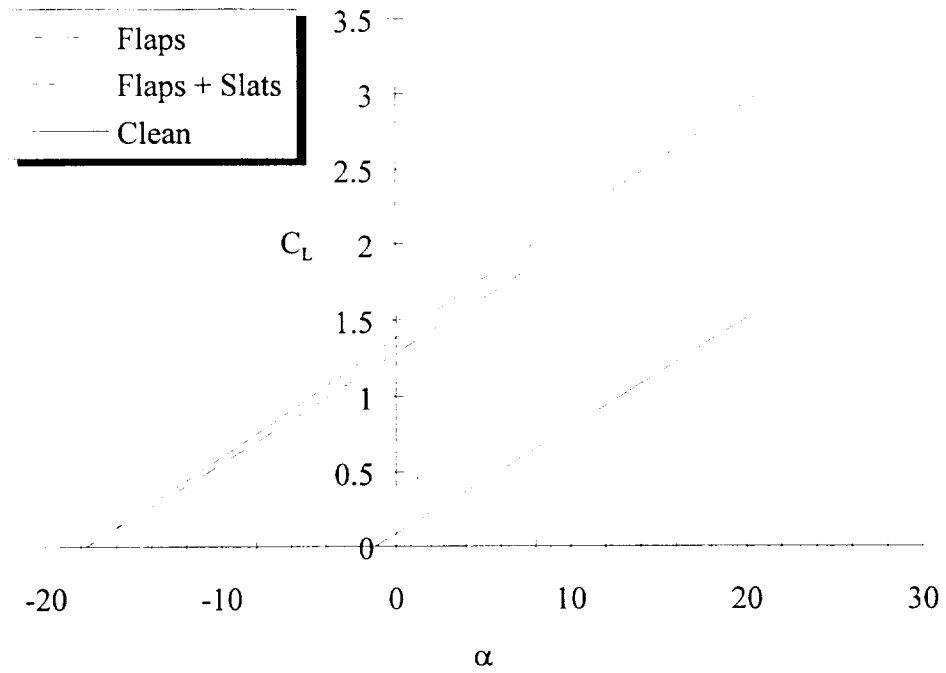


Figure 10.1 Lift Curves of Sample Test Cases

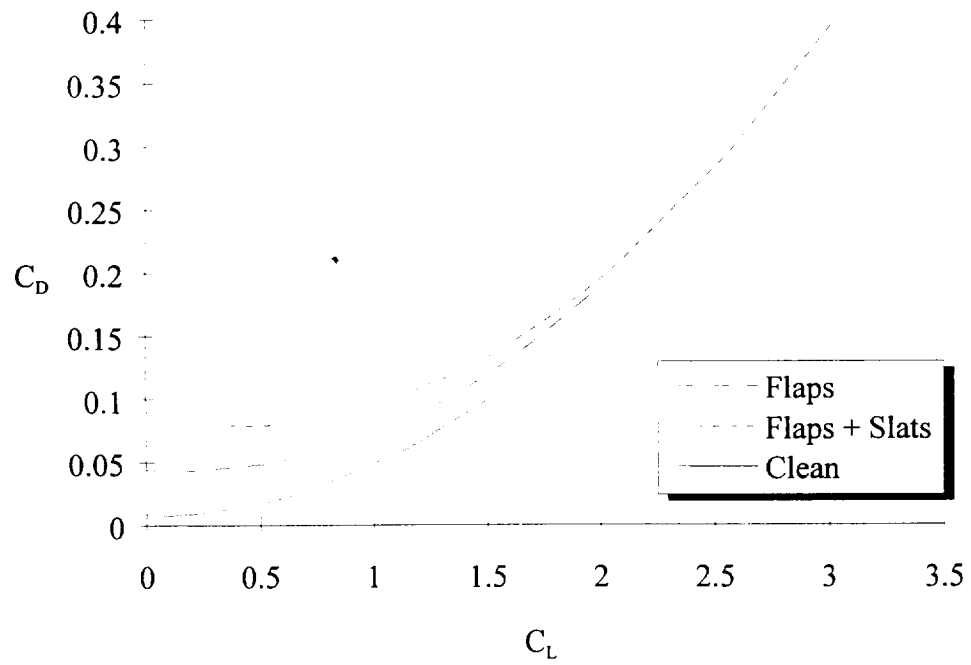


Figure 10.2 Drag Polars of Sample Test Cases

11.0 Concluding Remarks

Today's highly competitive market necessitates the ability to develop a high-lift system that allows a civil transport aircraft to meet the stringent FAR Part 25 takeoff and landing requirements with minimal direct operational cost. This presents a daunting task for designers, since the optimization of a high-lift system is extremely complex. This report presents a comprehensive design methodology which includes aerodynamic performance, structural weight considerations, system complexity, and cost to be used within an aircraft conceptual design tool such as ACSYNT. Thus, aircraft performance and cost can be analyzed in parallel to select the optimal configuration.

Similar methodologies have been created in the past, but they should not be used today for two reasons. The methods generally consist of outdated experimental data, and the data is based on low Reynolds numbers. Today, CFD offers the best alternative, since it would be too costly to generate a large high-Reynolds-number experimental database as was done in the past. Computational methods can accurately, yet inexpensively, predict the flow field around multi-element airfoils in a reasonably short period of time. However, the most important advantage of using CFD is that airfoils can be analyzed at realistic flight Reynolds numbers.

CFD was the primary tool used in this research project to construct a database consisting of the NLR-7301 two-element and the Douglas LB-546 three-element airfoils. However, supplemental configurations such as a double-slotted and triple-slotted flap

must be added to build a more comprehensive database. This can be done without difficulty, since the new design methodology is easily extensible.

From this database empirical equations were constructed which are used to calculate two-dimensional aerodynamic coefficients. A spanwise lift distribution is then determined from a modified lifting-line theory using the two-dimensional data as input. Thus the total lift, drag, pitching moment, and maximum lift of the wing can be computed faster than with a panel method while incorporating the viscous effects of slotted high-lift devices.

Since the design methodology was intended to be used in an optimization routine, a reasonable compromise between CPU requirements and the accuracy of the predictions had to be found. Consequently, some assumptions and simplifications were made. One such simplification rests in the prediction of weight using historical data. Although this technique offers a consistent approach for predicting weight, it is a very simple method. Further research should be conducted to consider a method which incorporates loading information from CFD with slender beam analysis to determine the optimal weight of a configuration.

This methodology also neglects spanwise viscous flow effects since it employs a modified lifting-line method. Clearly, this problem cannot be solved until full 3-D viscous flow solutions become practical. Using the three-dimensional Reynolds-averaged Navier-Stokes (RaNS) equations will not only account for spanwise effects, but will also allow for inverse wing design. Nevertheless, until the 3-D RaNS equations for multi-element wings at high-lift conditions can be solved in a reasonable time period (i.e. less

than a day) the methodology presented in this paper will be a useful tool in the development of high-lift systems on civil transport aircraft.

References

- 1 Smith, A. M. O., "Aerodynamics of High-Lift Aerfoil Systems," in Fluid Dynamics of Aircraft Stalling, AGARD CP102, Nov. 1972, pp. 10/1-27.
- 2 Smith, A. M. O., "High-Lift Aerodynamics," Journal of Aircraft, Vol. 12, No. 6, June 1975, pp. 501-530.
- 3 Garner, P. L., Meredith, P. T., and Stoner, R. C., "Areas for Future CFD Development as Illustrated by Transport Aircraft Applications," AIAA Paper 91-1527-CP, June 1991.
- 4 Myklebust, A. and Gelhausen, P., "Putting the ACSYNT on Aircraft Design," Aerospace America, Sept. 1994, pp. 26-30.
- 5 Woodward, D. S. and Lean, D. E., "Where Is High-Lift Today? - A Review of Past UK Research Programmes," in *High-Lift System Aerodynamics*, AGARD CP-515, Sept. 1993, pp. 1/1-45.
- 6 Wedderspoon, J. R. "The High Lift Development of the A320 Aircraft," ICAS 86-2.3.2, September 1986.
- 7 Flaig, A. and Hilbig, R., "High-Lift Design for Large Civil Aircraft," in *High-Lift System Aerodynamics*, AGARD CP-515, Sept. 1993, pp. 31/1-12.
- 8 Rogers, S. E., Wiltberger, N. L., and Kwak, D. "Efficient Simulation of Incompressible Viscous Flow Over Single- and Multi-Element Airfoils," Journal of Aircraft, Vol. 30, No. 5, Sept., 1993, pp. 736-743.
- 9 Rogers, S. E. and Kwak, D., "An Upwind Differencing Scheme for the Steady State Incompressible Navier-Stokes Equations," Journal of Applied Numerical Mathematics, Vol. 8, 1991, pp. 43-64.
- 10 Coa, H. V. and Kusunose, K., "Grid Generation and Navier Stokes Analysis for Multi-Element Airfoils," AIAA Paper 940748, Jan. 1994.
- 11 Mavriplis, D. J., "Turbulent Flow Calculations Using Unstructured and Adaptive Meshes," NASA CR 182102, Sept. 1990.

- 12 Mavriplis, D. J., "Unstructured Mesh Algorithms for Aerodynamic Calculations," in Fifth Symposium on Numerical and Physical Aspects of Aerodynamic Flows, California State University, Long Beach, CA, Jan. 1992.
- 13 Valarezo, W. O. and Mavriplis, D. J., "Navier-Stokes Applications to High-Lift Airfoil Analysis," AIAA Paper 933534, Aug. 1993.
- 14 Drela, M., "Newton Solution of Coupled Viscous/Inviscid Multi-Element Airfoil Flows," AIAA Paper 90-1470, June 1990.
- 15 Hardin, J. D., Potter, R. C., van Dam, C. P., and Yip, L. P., "Two-Dimensional Computational Analysis of a Transport High-Lift System and Comparison with Flight-Test Results," AIAA Paper 93-3533, Aug. 1993.
- 16 Rogers, S. E., Menter, F. R., Durbin, P. A., and Mansour, N. N., "A Comparison of Turbulence Models in Computing Multi-Element Airfoil Flows," AIAA Paper 94-0291, Jan. 1994.
- 17 Vinh, H., van Dam, C., Yen, D., and Pepper, R., "Drag Prediction Algorithms for Navier-Stokes Solutions About Airfoils," AIAA Paper 95-1788, June 1995.
- 18 van den Berg, B., "Boundary Layer Measurements on a Two-Dimensional Wing with Flap," National Aerospace Laboratory TR-79009 U, The Netherlands, January 1979.
- 19 Lin, J. C. and Dominik, C. J., "Optimization of An Advanced Design Three-Element Airfoil at High Reynolds Numbers," AIAA Paper 95-1858, June 1995.
- 20 Lean, D. E. and Fiddes, S. P., "A Rapid Method for Estimating Equivalent Parabolic Polars from Wind-Tunnel Test," RAE Tech. Memo AERO 2034, April 1985.
- 21 Kusunose, K. and Cao, H., "Prediction of Transition Location for a 2-D Navier-Stokes Solver for Multi-Element Airfoil Configurations," AIAA Paper 94-2376, June 1994.
- 22 Weissinger, J., "The Lift Distribution of Swept-Back Wings", NACA TM 1120, 1947.
- 23 Hoak, D., "USAF Stability and Control Datcom", Flight Control Division, Air Force Flight Dynamics Laboratory, WPAFB, Ohio, 45433-0000, 1978, revised.
- 24 Schlichting, H. and Truckenbrodt, E., Aerodynamics of the Airplane, McGraw-Hill, 1979.

- 25 Roshko, A. "Computation of the Increment of Maximum Lift Due to Flaps," Douglas Aircraft Co. Report SM-23626, 1959.
- 26 Moran, J., An Introduction to Theoretical and Computational Aerodynamics, John Wiley & Sons, 1984.
- 27 Holbrook, G. and Dunham, D., "Detailed Pressure Distribution Measurements Obtained on Several Configurations of an Aspect Ratio-7 Variable Twist Wing," NASA TM 86308, 1985.
- 28 Hunton, L. W., "Effects of Twist and Camber on the Low-Speed Characteristics of a Large-Scale 45° Swept-Back Wing," NASA RM A50A10, 1950.
- 29 Valarezo, W. and Chin, V., "Method for the Prediction of Wing Maximum Lift," *Journal of Aircraft*, Vol. 31, No. 1, Jan. 1994, pp. 103-109.
- 30 Ljungström, B. L. G. "Two-Dimensional Wind Tunnel Experiments with Single and Double Slotted Flaps," FFA Technical Note AU-1083, Oct. 1975.
- 31 Murillo, L. and McMasters, J., "A Method for Predicting Low-Speed Aerodynamic Characteristics of Transport Aircraft," *Journal of Aircraft*, Vol. 21, No. 3, March 1984, pp. 168-174.
- 32 Vanderplaats, G., Numerical Optimization Techniques for Engineering Design: with Applications, McGraw-Hill, 1984.
- 33 Anderson, R., Flora, C., Nelson, R., Raymond, E., and Vincent, J., "Development of Weight and Cost Estimates for Lifting Surfaces with Active Controls," NASA CR-144937, March 1976.
- 34 Oman, B. H., "Vehicle Design Evaluation Program," NASA CR-145070, Jan. 1977.
- 35 Anderson, R., Flora, C., Nelson, R., Raymond, E., and Vincent, J., "Development of Weight and Cost Estimates for Lifting Surfaces with Active Controls," NASA CR-144937, March 1976.
- 36 Ardema, M. et al., "Analytical Fuselage and Wing Weight Estimation of Transport Aircraft," Oct. 1995.
- 37 Yip, L. P., et al., "The NASA B737-100 High-Lift Research Programme-Measurements and Computations," *Aeronautical Journal*, Nov. 1995, pp. 372-386.
- 38 Gelhausen, P., Personal Communication, Jan. 1996.

- 39 Rudolph, P., Personal Communication, Sep. 1995.
- 40 Anon., "Simpler 737 Flap Design," Aviation Week & Space Technology, April 18, 1994, p. 38.

Appendix A

Spanwise Load Distribution Calculations of a Wing with Arbitrary Plan Form Using the Weissinger Method

Summary

The application of Weissinger's theory is shown for calculating the spanwise loading across a wing. From this procedure a spanwise load distribution can be calculated for a wing of arbitrary plan form from a 2-D lift curve slope and angle of zero lift. The geometry of the wing may be asymmetric about the centerline and can include sweep, taper, or twist. Partial span flaps may be modeled as discontinuities in twist. Fowler motion can also be modeled as an increase in chord length. Lift, induced drag, pitching moment, and induced angle of attack may then be calculated.

Method

The Weissinger method models the wing as a plate of zero thickness, but the planform and twist remain identical to the actual wing. The chordwise load distribution at each span station is concentrated into a lifting line located at the wing's quarter-chord line. The theory requires that the quarter chord line is straight, however a discontinuity is allowed at the plane of symmetry so that a swept wing may be considered.

The method assumes that the lifting line and its trailing vortex sheet are continuous. However, discrete values for the circulation strength are determined only at the span stations along the quarter-chord line corresponding with control points. The

number of control points, m , is specified, and each is placed at the three-quarter-chord line. Mathematically this implies that the lift curve slope is $2\pi \text{ rad}^{-1}$, and a correction method must be incorporated for a lift curve slope that varies from the theoretical value.

The boundary conditions specify that the induced angle of attack due to the downwash of the trailing vortex is equal to the angle of attack of the plate. This ensures tangency of the flow to the plate at each control point.

Substituting the wing with a bound vortex system and applying the boundary conditions enables the formation of a set of simultaneous equations. Each of these equations is a function of the angle of attack of the wing, the load coefficient $G_j = \frac{C_l c}{2b}$ at each span station j on the quarter-chord line, and the influence coefficients A_{ij} which are only a function of geometry and relate the influence of the circulation at any point j along the lifting line to the downwash at any control point i . The distribution of the load G_j may then be calculated from the set of m simultaneous equations.

$$\alpha_i = \sum_{j=1}^m A_{i,j} G_j, \quad i = 1, 2, 3, \dots, m \quad (\text{A-1})$$

where

$$\alpha_i = \frac{w_i}{V_\infty} = (\alpha_{\text{wing}} - \alpha_o)_i \quad (\text{A-2})$$

Each equation gives the downwash angle at the control point $\eta = \cos\phi_i$ resulting from the circulation effects of m points along the span.

The following trigonometric substitutions are used to define span locations at the control points or on the lifting line respectively,

$$\text{---} \tag{A-3}$$

$$\text{---} \tag{A-4}$$

==== coefficients are shown below.

$$\text{---} \tag{A-5}$$

$$\text{---} \tag{A-6}$$

$$\text{---} \tag{A-7}$$

$$\frac{\text{---}}{\text{---} \cos^2 \phi_1} \frac{1 - (-1)^{j-i}}{2(m+1)} \tag{A-8}$$

==== coefficients are given as

$$\frac{L_{i,0} f_{j,0} + L_{i,M+1} f_{j,M+1} + \sum_{k=1}^M L_{i,k} f_{j,k}}{2} \tag{A-9}$$

==== of span stations used to integrate the downwash and does not have

==== The subscripts 0 and M+1 denote values for k. Also note that

$$\text{---} \tag{A-10}$$

==== and coefficients $L_{i,k}$ are defined as follows:

$$\text{---} \tag{A-11}$$

$$\bar{\eta} = \cos \frac{k\pi}{m+1} \quad (\text{A-12})$$

for $\bar{\eta} \leq 0$

$$L_{i,k} = \frac{1}{(b/c)(\eta - \bar{\eta})} \left\{ \frac{\sqrt{[1 + (b/c)(|\eta| + \bar{\eta}) \tan \Lambda]^2 + (b/c)^2 (\eta - \bar{\eta})^2}}{1 + (b/c)(|\eta| + \eta) \tan \Lambda} - 1 \right\} \\ + \frac{2 \tan \Lambda \sqrt{[1 + (b/c)|\eta| \tan \Lambda]^2 + (b/c)^2 \eta^2}}{[1 + (b/c)(|\eta| - \eta) \tan \Lambda][1 + (b/c)(|\eta| + \eta) \tan \Lambda]} \quad (\text{A-13})$$

for $\bar{\eta} \geq 0$

$$L_{i,k} = \frac{1}{(b/c)(\eta - \bar{\eta})} \left\{ \frac{\sqrt{[1 + (b/c)(|\eta| - \bar{\eta}) \tan \Lambda]^2 + (b/c)^2 (\eta - \bar{\eta})^2}}{1 + (b/c)(|\eta| - \eta) \tan \Lambda} - 1 \right\} \quad (\text{A-14})$$

The mathematical series coefficients $f_{j,k}$ are used in a numerical integration method and are shown below:

$$\phi_k = \cos \frac{k\pi}{M+1} \quad (\text{A-15})$$

$$f_{j,k} = \frac{2}{m+1} \sum_{\mu=1}^m \mu \sin \mu \phi_j \cos \mu \phi_k \quad (\text{A-16})$$

Sectional Lift curve Slope Correction

The Weissinger method assumes that the lift curve slope is $2\pi \text{ rad}^{-1}$. This implies that the control points lie along the three-quarter-chord line. When considering airfoils with lift curve slopes that vary from this theoretical value (as a result of viscous, compressibility, or geometry effects), a correction method must be incorporated. This

involves moving the control points from the three-quarter-chord line; but before this is done a derivation of this location will be shown.

The velocity induced by an infinite vortex of strength Γ and distance h is given as

$$w = \frac{\Gamma}{2\pi h} \quad (\text{A-17})$$

and the sectional lift coefficient is related to the circulation strength as follows:

$$\rho V_\infty \Gamma = \frac{1}{2} \rho V_\infty^2 c C_l \quad (\text{A-18})$$

Rearranging these two equations and combining them yields

$$C_l = 4\pi \frac{w}{V_\infty} \frac{h}{c} \quad (\text{A-19})$$

Since $\alpha = \frac{w}{V_\infty}$ the above equation can be rewritten as

$$\frac{C_l}{\alpha} = 4\pi \frac{h}{c} \quad (\text{A-20})$$

If the lift curve slope is assumed to be 2π then it can be shown that $\frac{h}{c}$ must be $\frac{1}{2}$. Then

the point at which no flow passes through the plate occurs at $\frac{1}{2}c$ from the lifting line or

at the three-quarter-chord line.

If the lift curve slope deviates from the theoretical value each control point location must be modified. This means that each control point must be moved forward of the three-quarter-chord line if the slope is less than $2\pi \text{ rad}^{-1}$ or must be moved rearward if it is greater. This variation can also be modeled as a change in the value of $\frac{b}{c_v}$ by the

ratio of the experimental lift curve slope to the theoretical lift curve slope $\frac{C_{l\alpha_{exp}}}{2\pi/\beta}$ at the desired Mach number, M , where $\beta = \sqrt{1 - M^2}$. The modified geometry can be expressed as

$$\left(\frac{b}{c_v}\right)_{mod} = k_v \frac{b}{c_v} \quad (A-21)$$

where

$$k_v = \frac{C_{l\alpha_{exp}}}{2\pi/\beta} \quad (A-22)$$

Caution should be taken when large deviations in the lift curve slope are used. The method does not rigorously allow such modifications, and the accuracy of the results may deteriorate for large angles of sweep.

Compressibility Correction

Compressibility effects are included with the aid of the Prandtl-Glauert rule. It approximates the effects of compressibility as an increase in the local chord and sweep

angle by the factor $\frac{1}{\beta}$.

$$\left(\frac{b}{c_v}\right)_\beta = \frac{1}{\beta} \frac{b}{c_v} \quad (A-23)$$

$$\Lambda_\beta = \tan^{-1}\left(\frac{\tan \Lambda}{\beta}\right) \quad (A-24)$$

Thus the span loading for the original plan form at a given Mach number can be calculated for an incompressible flow using a modified geometry.

Aerodynamic Characteristics

The circulation strength is calculated directly from the dimensionless load coefficient and has the dimensions [ft²/s].

$$\Gamma_v = bV_\infty G_v \quad (\text{A-25})$$

The sectional lift coefficient is also calculated from the load coefficient as

$$C_{l_v} = 2 \frac{b}{c_v} G_v \quad (\text{A-26})$$

The total lift coefficient is determined from

$$C_L = \frac{\pi AR}{m+1} \sum_{v=1}^m G_v \sin \phi_v \quad (\text{A-27})$$

The induced angle of attack at the quarter-chord point of station v is given by

$$\alpha_{i_v} = b_{vv} G_v - \sum_{n=1}^m {}' b_{vn} G_n \quad (\text{A-28})$$

where the primed summation sign indicates that the value for $n = v$ is not summed. The total induced drag is calculated from

$$C_{D_i} = \frac{\pi AR}{m+1} \sum_{v=1}^m G_v \alpha_{i_v} \sin \phi_v \quad (\text{A-29})$$

Appendix B

Weight Estimation of Other Control Surfaces

Like leading and trailing-edge device weights, the estimation of aileron and spoiler weights is based on historical data of existing aircraft. Similarly, the total system weights are broken up into components of surface, support, and actuation. The weight estimation equations given below are only a function of the planform area of the representative control surface.

Aileron Weight

Surface Weight:

$$W_{\text{surf}} = 5.5 \cdot S_{\text{ail}} \quad (\text{B-1})$$

Support Weight:

$$W_{\text{supp}} = 0.74 \cdot S_{\text{ail}} \quad (\text{B-2})$$

Actuation Weight:

$$W_{\text{act}} = 4.3 \cdot S_{\text{ail}} \quad (\text{B-3})$$

Total Aileron Weight:

$$W_{\text{ail}} = W_{\text{surf}} + W_{\text{supp}} + W_{\text{act}} \quad (\text{B-4})$$

Spoiler Weight

Surface Weight:

$$W_{\text{surf}} = 110 + 1.65 \cdot S_{\text{sp}} \quad (\text{B-5})$$

Support Weight:

$$W_{\text{supp}} = 1.3 \cdot S_{\text{sp}} \quad (\text{B-6})$$

Actuation Weight:

$$W_{\text{act}} = 270 + 1.35 \cdot S_{\text{sp}} \quad (\text{B-7})$$

Total Spoiler Weight:

$$W_{\text{sp}} = W_{\text{surf}} + W_{\text{supp}} + W_{\text{act}} \quad (\text{B-8})$$

Appendix C

High-Lift Weight Data of Various Aircraft (All weights are in pounds.)

Trailing-Edge Device Weight Data

Weight	Boeing 727-200			Boeing 737-200			Boeing 747-21P			Boeing 757-200			Boeing 767			DC-8 Model 62F			MD-83			MD-11				
	inboard	outboard	total	inboard	outboard	total	inboard	outboard	total	inboard	outboard	total	inboard	outboard	total											
Surface	657	562	1196	353	432	785	2491	1713	3516	1518	962	1422	1804	807	1478	2285	—	—	—	1293	1605	1885	3493	—	—	
Supports	1391	769	1703	411	473	884	5168	2732	7519	1549	1427	979	2406	983	83	1066	—	—	—	198	—	—	1816	—	—	
Fairings	—	—	291	56	108	164	1319	654	1582	392	159	170	329	—	—	—	—	—	—	59	191	213	404	—	—	
Controls	—	—	934	—	—	722	—	—	2170	722	—	—	—	—	—	370	—	—	—	241	—	—	597	—	—	
Total			4124			2555			16787			4181			3721			1790			1790			6308		
Nested Area, S_{TE}			281			175			847			327		173	236	409			456.9			210.8			668.2	
Weight / S_{TE}																										
Surface	—	—	4.26	—	—	4.49	—	—	6.31	—	—	4.64	—	3.56	3.57	4.41	—	—	5.00	—	—	6.13	—	—	5.22	
Supports	—	—	6.06	—	—	5.05	—	—	8.88	—	—	4.74	—	8.25	4.15	5.88	—	—	2.33	—	—	0.94	—	—	2.72	
Fairings	—	—	1.04	—	—	0.94	—	—	1.87	—	—	1.20	—	0.92	0.72	0.80	—	—	—	—	—	0.28	—	—	0.60	
Controls	—	—	3.32	—	—	4.13	—	—	2.56	—	—	2.21	—	—	—	—	—	—	0.81	—	—	1.14	—	—	0.89	
Total			14.68			14.60			19.82			12.99			8.14			8.14			8.49			9.44		

Leading-Edge Device Weight Data

Weight	Boeing 727-200			Boeing 737-200			Boeing 747-21P			Boeing 757-200			Boeing 767			DC-8 Model 62F			MD-83			MD-11		
	inboard	outboard	total	inboard	outboard	total	inboard	outboard	total	inboard	outboard	total	inboard	outboard	total	inboard	outboard	total	inboard	outboard	total	inboard	outboard	total
Surface	252	900	752	127	272	399	379	1130	1509	—	—	—	—	—	—	597	0	397	652	0	652	423	1591	2014
Support	0	214	214	0	100	100	90	707	797	—	—	—	—	—	—	0	0	0	937	0	937	488	1834	2322
Controls	—	—	—	—	—	232	—	—	1252	—	—	—	—	—	—	—	—	148	—	—	1003	—	—	1461
Total			1314			731			3538							745			2592			5797		
Nested Area, S_{LE}	55	145	200	24.3	76.1	100.6	122	326	448			198			304.6			120.8	0.0	120.8	100.3	371.6	471.9	
Weight / S_{LE}																								
Surface	4.58	3.45	3.76	5.23	3.56	3.97	3.11	3.47	3.37	—	—	—	—	—	—	5.40	—	5.40	4.22	—	4.28	4.27	—	4.27
Supports	0.00	1.48	1.07	0.00	1.31	0.99	0.74	2.17	1.78	—	—	—	—	—	—	7.76	—	7.76	4.86	—	4.94	4.92	—	4.92
Controls	—	—	1.74	—	—	2.31	—	—	2.79	—	—	—	—	—	—	—	—	8.30	—	—	—	—	—	3.10
Total			6.57			7.27			7.94															

Fixed Structure Weight Data

Weight	B-727	B-737	B-747	B-757	B-767	DC-8	MD-83	MD-11
Trailing Edge	648	370	1833	—	—	—	1351	871
Leading Edge	817	402	4000	—	—	—	577	2213

Aileron Weight Data

Weight	B-727	B-737	B-747	B-757	B-767	DC-8	MD-83	MD-11
Surface	344	137	908	—	—	2519	35913	1021
Support	43	16	166	—	—	1	38.61	229.55
Controls	291	226	1009	—	—	427	109.73	582.27
Total	678	379	2083			2947	30747	1832.82
Aileron Area, S_{ail}	57	26.9	226	48	124.6	161.6	38	187.8
Weight / S_{ail}								
Surface	6.04	5.09	4.02	—	—	15.59	9.45	5.44
Supports	0.75	0.59	0.73	—	—	0.01	1.02	1.22
Controls	5.11	8.40	4.46	—	—	2.64	2.89	3.10
Total	11.89	14.07	9.22			18.24	13.35	9.76

Spoiler Weight Data

Weight	B-727	B-737	B-747	B-757	B-767	DC-8	MD-83	MD-11
Surface	312	156	582	—	—	—	—	39
Support	—	—	391	—	—	—	132.77	175.12
Controls	460	290	680	—	—	—	327.26	501.8
Total	792	446	1653				461.53	1035.92
Nested Area, S_{sp}	79.8	45.1	304	256	170.4	48.5	34.7	137
Weight / S_{sp}								
Surface	4.16	3.46	1.91	—	—	—	0.00	2.62
Supports	0.00	0.00	1.29	—	—	—	3.83	1.28
Controls	5.76	6.43	2.24	—	—	—	9.45	3.66

Appendix D

Database Formulation

The first step in integrating a database into the high-lift module is to formulate the data based on important parameters. This has already been done, and the empirical equations can be found in the documentation. The second step is to determine appropriate empirical coefficients for the formulas. This has been completed for leading-edge devices and single-slotted trailing-edge flaps but can be done for other configurations by finding the empirical coefficients which minimize the error between the predictions and the actual data. In other words, iterate on the empirical coefficients to minimize the RMS:

$$\text{RMS} = \sqrt{\text{average}(\text{predicted values} - \text{database values})^2}$$

The empirical equations for χ , $\Delta C_{d_{\min}}$, $\Delta C_{l_{\min}}$, Δk_p , $C_{l_{\delta_{\max}}}$, and x_{cp} are given in equations 11, 26, 27, 28, 62, and 41 respectively and must be fit to a new configuration data set in order to integrate the new configuration. The database values of these parameters are determined from the CFD data as follows:

$$\alpha_{\delta} = \frac{\Delta C_{l_{TE}}}{C_{l_{\alpha_{\text{clean}}}} \delta_{TE} \frac{c'}{c}} \quad (\text{Find } \chi \text{ which accurately predicts}$$

α_{δ} .)

$$\Delta C_{l_{TE}} = C_l - C_{l_{\text{clean}}}$$